J. Fluid Mech. (1987), *vol.* 185, *pp.* 569–598
Printed in Great Britain

The boundary layer due to a three-dimensional vortex loop

By S. ERSOY† AND J. D. A. WALKER
Department of Mechanical Engineering and Mechanics, Lehigh University, Bethlehem, PA 18015, USA

(Received 14 January 1986 and in revised form 5 June 1987)

The nature of the boundary layer induced by the motion of a three-dimensional vortex loop towards a plane wall is considered. Initially the vortex is taken to be a ring approaching a plane wall at an angle of attack in an otherwise stagnant fluid; the ring rapidly distorts into a loop shape due to the influence of the wall and the trajectory is computed from a numerical solution of the Biot–Savart integral. As the vortex loop moves, an unsteady boundary-layer flow develops on the wall. A method is described which allows the computation of the flow velocities on and near the symmetry plane of the vortex loop within the boundary layer. The computed results show the development of a variety of complex three-dimensional separation phenomena. Some of the solutions ultimately show strong localized boundary-layer growth and are suggestive that a boundary-layer eruption and a strong viscous–inviscid interaction will be induced by the moving vortex.

1. Introduction

Physical situations involving the motion of vortices near solid walls occur in a variety of diverse circumstances in fluid mechanics. As a vortex moves above a wall, it induces an unsteady flow in the viscous boundary layer near the wall and it is of interest to understand the nature of this viscous response to the vortex motion. In many situations, the induced boundary-layer effects have a profound influence on the vortex motion. In the case of aircraft trailing vortices, it is known (Harvey & Perry 1971; Walker 1978) that each trailing vortex actuates a strong boundary-layer eruption as the vortex approaches the ground plane. The phenomenon initiates because the vortex induces an adverse pressure gradient on a portion of the unsteady boundary-layer flow near the ground; an unsteady separation, in the form of a detached secondary eddy, develops within the boundary layer and this is soon accompanied by explosive boundary-layer growth near the separation (Walker 1978). The process culminates in a strong viscous–inviscid interaction consisting of an abrupt ejection of a secondary vortex from the boundary layer. The secondary vortex is of opposite rotation to the original trailing vortex and is strong enough that the trajectory of the trailing vortex is substantially changed from that predicted by inviscid theory (Harvey & Perry 1971).

The boundary-layer effects induced by two-dimensional vortex have been considered by Doligalski & Walker (1984) for a vortex convected in a uniform flow above a wall and by Ersoy & Walker (1985*a*, *b*, 1986) for counter-rotating vortex pairs near a wall. Numerical calculations for the development of such flows reveal

† Present address: 9 Eylül University, Izmir, Turkey.

that a variety of complex and unusual separation phenomena occur in the boundary layer as a consequence of the adverse pressure gradient imposed by the vortex motion above. However one common conclusion is that once two-dimensional vortices are close enough to a wall for a sufficient period of time, a boundary-layer eruption and a strong interaction with the outer inviscid flow is apparently inevitable.

The results for two-dimensional flows are suggestive of the basic physical mechanisms in more complex three-dimensional flows. For example, the solutions for vortex pairs (Ersoy & Walker 1985*a*) suggest a reasonable explanation of why a Görtler-vortex flow develops secondary instabilities (Bippes 1972). The basic phenomenon also offers a potential explanation for the observed regeneration of vorticity in turbulent boundary layers (Walker, Scharnhorst & Weigand 1986). However, an additional feature of three-dimensional motion which may have an important effect is the phenomenon of vortex stretching. Perhaps the simplest illustration of vortex stretching corresponds to a circular vortex ring approaching a wall on a trajectory normal to the wall; as the ring moves towards the wall, the diameter expands and at the same time, the dimensions of the vortex core decrease, giving rise to an intensification of the level of vorticity near the core (Lamb 1932, p. 242). It emerges that in this case, vortex stretching appears to enhance the eruptive response from the boundary-layer flow near the wall; a series of detailed experimental and numerical studies carried out by Walker *et al.* (1987) show that a moving vortex ring induces the formation of a secondary vortex ring within the boundary layer and that the secondary ring is subsequently ejected from the boundary layer. In many cases, the original ring was able to induce the formation of a third tertiary ring. Similar results have recently been reported by Didden & Ho (1985) who have investigated the flow near a wall due to a forced impinging air jet. The jet was oriented normal to the wall and contained ring vortices on the periphery of the jet. The vortices were observed to induce several unsteady separations in the boundary-layer flow near the wall and eruptions in the form of ejections of secondary vortices.

Vortex motions are known to be an important feature of the time-dependent flow in a turbulent boundary layer and at least two different types of relevant vortex models have been proposed. The first of these is the hairpin vortex (Head & Bandyophadyay 1981; Smith 1984; Acalar & Smith 1984, 1987*a*, *b*; Hon & Walker 1987). Another type of vortex motion has also been proposed as a potential basic element of wall-layer turbulence; this is the discrete loop vortex (Doligalski & Walker 1978; Falco 1977, 1982, 1983) which is the subject of this study. In theory, all vortex filaments form a closed loop in three-dimensional flows since the no-slip condition prohibits the termination of a vortex filament on a solid wall in a real fluid. The observation of what appear to be small compact ring-like vortices in wall-layer turbulence (Falco 1977, 1982) has led R. E. Falco (1979, private communication), Falco & Wiggert (1980) and Cerra & Smith (1983) to investigate the nature of the viscous flow created by a ring vortex which was set in motion towards a plane wall at an angle of attack; these flow visualization experiments showed that a complex interaction occurred as the vortex approached the wall which resulted in the creation and subsequent ejection of a secondary vortex from the boundary layer on the wall. An objective of the present study is to compute the type of boundary-layer development that has been observed in these studies.

In the configuration considered here, the vortex is taken to be a circular vortex ring which is introduced into an otherwise stagnant fluid above an infinite plane wall;

as time increases, the ring distorts into a three-dimensional loop due to the influence of the plane wall. The vortex is assumed to be a filament of small cross-sectional area. To calculate the subsequent motion it is necessary to track the evolution of a three-dimensional space curve and this was carried out through a numerical time-dependent integration of the Biot–Savart law using an approach developed by Moore (1972). As the vortex loop moves, it induces an unsteady three-dimensional boundary-layer flow near the wall. For vortex-driven boundary-layer flows in two-dimensions (see for example Doligalski & Walker 1984), on the order of 2×10^4 mesh points were required to provide an accurate description of the complex flows that develop in the boundary layer; it is certain that this figure would have to be increased by at least two orders of magnitude to compute the full three-dimensional flows of interest in the present study. Such a computation would require larger computer resources than were available and consequently a simplification of the boundary-layer problem was considered.

In the present configuration, the vortex loop always has a plane of symmetry as it moves either towards or away from the wall. It emerges that the boundary-layer flow on the plane of symmetry develops independently of the rest of the boundary-layer flow. Here an approach is developed that allows for the computation of the leading terms for all three velocity components in the boundary layer on and near the symmetry plane. Calculations are carried out for three cases; of these, two are situations where the vortex moves towards the wall whereas in the third case the vortex recedes from the wall. As the vortex loop moves, the unsteady boundary-layer development near the symmetry plane is computed numerically. In all cases, boundary-layer separation and a complex flow evolution occur on the symmetry plane. In the two cases where the vortex moves towards the wall, separation is soon followed by an explosive local boundary-layer growth. The results suggest that a strong interaction will occur in the form of the ejection of a secondary vortex from the boundary layer and here the correspondence with experimental observation is encouraging.

In §2 the numerical approach and theory needed to compute the trajectory of the vortex loop are described. The boundary-layer problem for the flow in and near the symmetry plane is formulated in §3; the asymptotic form of the boundary-layer problem on the symmetry plane but at large distances from the vortex loop is derived in §4. The numerical solution method for the boundary-layer problem is discussed in §5 and calculated results are described in §6. A summary of results is given in §7.

2. The inviscid flow

Consider the initial configuration depicted in figure 1 where a vortex ring of radius R is located above a plane wall; (x, y, z) are dimensionless Cartesian coordinates (with respect to R) having origin in the plane and with y measuring distance normal to the plane. Initially the normal to the plane of the vortex ring intersects the (x, z)-plane at an angle of attack α; the projection of this normal defines the streamwise x-direction. A sketch of the initial vortex configuration as projected into the (x, z)-plane is given in figure 2 and it may be inferred that the inviscid flow induced by the ring and its image below the wall is symmetric about the (x, y)-plane. The coordinate z measures spanwise distance from the symmetry plane $z = 0$. The vortex ring cuts the symmetry plane in two locations which have coordinates that will be denoted by $(x_1, y_1, 0)$ and $(x_2, y_2, 0)$; the slice of the vortex closest to the wall is always designated as $(x_2, y_2, 0)$. The schematic diagrams in figures 1 and 2 apply only at the initial

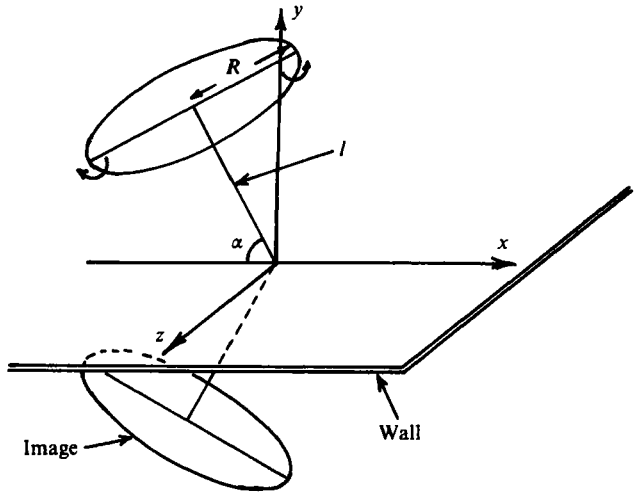

FIGURE 1. The geometry and initial configuration of the vortex ring.

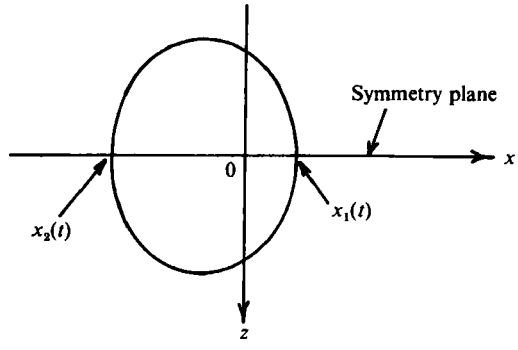

FIGURE 2. Top view of the initial vortex configuration.

instant. The ring will start to deform immediately under the influence of the velocity field due to the image vortex below the plane, into a shape that will be referred to as a loop. Depending on the assumed sense of circulation the loop vortex will either advance towards the wall or recede from it. However it is evident that, even as the vortex deforms and (x_1, y_1) and (x_2, y_2) change with time, the inviscid flow remains symmetric about the plane $z = 0$.

The evolution of the vortex was computed using the Biot–Savart law for which a variety of approaches are possible (Leonard 1980, 1985). The method described by Moore (1972) is particularly convenient for numerical calculations (see also Dhanak & De Bernardinis 1981; Dhanak 1981) and the specific form is

$$\boldsymbol{u}^*(s_0, t^*) = \frac{\Gamma}{4\pi R} \oint_C \frac{\partial \boldsymbol{X}}{\partial s} \wedge \frac{\{\boldsymbol{X}(s_0, t^*) - \boldsymbol{X}(s, t^*)\}}{\{|\boldsymbol{X}(s_0, t^*) - \boldsymbol{X}(s, t^*)|^2 + \mu^2\}^{\frac{3}{2}}} \mathrm{d}s + \boldsymbol{u}^*_{\mathrm{ext}}, \tag{1}$$

where s is a Lagrangian coordinate along the space curve C defining the instantaneous location of the vortex and s_0 denotes a specific location on the vortex; $\boldsymbol{u}^*$ is the velocity vector at s_0, $\boldsymbol{u}^*_{\mathrm{ext}}$ is an external irrotational flow field due to the image vortex and t^* is dimensional time. Here Γ is the circulation about the vortex in a plane

normal to the filament and, by Kelvin's theorem (Batchelor 1970), is constant both in time and along the vortex. The integrand in the Biot–Savart integral is generally singular at $s = s_0$ and the consequent velocity field must be interpreted as an outer solution, which is singular near the vortex and which must be matched to an inner viscous solution in the vortex core (Callegari & Ting 1978). In Moore's (1972) method, a small parameter μ is inserted into the denominator of the integrand in (1) to artificially make the integrand finite at $s = s_0$; by evaluating (1) when C is a circular vortex ring (Moore 1972; Ersoy & Walker 1985*b*) moving in an otherwise stagnant fluid and by insisting that the resulting expression agree with known exact results obtained from asymptotic matching, it can be shown that μ is proportional to the vortex-core radius a. For a vortex core in solid-body rotation and having no axial flow, it may be verified (Moore 1972) that this procedure leads to

$$\mu = \mathrm{e}^{-\frac{3}{4}} a. \tag{2}$$

At any stage in the motion, the vortex-core radius is sensibly uniform along the vortex (Moore & Saffman 1972; Callegari & Ting 1978) and

$$L(t^*)\, a^2(t^*) = 2\pi a_0^2. \tag{3}$$

where a_0 is the initial core radius and $L(t^*)$ is total arc length of the vortex filament at time t^*. From a physical standpoint, any local non-uniformities in the core radius are rapidly smoothed out by internal waves which travel along the vortex core in a timescale that is short with respect to the overall motion of the vortex (Moore & Saffman 1972).

At $t^* = 0$, the Lagrangian s-coordinate was chosen to have a range $(-1, 1)$ on the initial ring vortex with $s = 0$ corresponding to the front portion of the vortex on the symmetry plane and $s = \pm 1$ defining the rear portion on $z = 0$. Calculations were carried out for s in the range $(0, 1)$ (by virtue of the symmetry about $s = 0$) using a number of mesh sizes as a check on the accuracy. A typical calculation involved 100 equal intervals for s in the range $[0, 1]$. Note that $s =$ constant always refers to the same fluid particle whose position is then tracked in space with the passage of time.

The specific value of the circulation Γ may be scaled out of the equations by defining a dimensionless time and velocities according to

$$t = \frac{|\Gamma|\, t^*}{2\pi R^2}, \quad \boldsymbol{u} = \frac{2\pi R \boldsymbol{u}^*}{|\Gamma|}. \tag{4}$$

The circulation Γ is positive in the configuration depicted in figure 1, for which the vortex will move towards the wall; for Γ negative, the vortex recedes from the wall. Each node of the vortex is convected in the induced velocity field and with $\boldsymbol{u} = \partial \boldsymbol{X}/\partial t$, (1) governing the vortex trajectory may be written

$$\frac{1}{\mathrm{sgn}\,(\Gamma)} \frac{\partial \boldsymbol{X}}{\partial t}(s_0, t) = \frac{1}{2} \int_{-1}^{1} \left[\frac{\partial \boldsymbol{X}}{\partial s} \wedge \frac{\{\boldsymbol{X}(s_0, t) - \boldsymbol{X}(s, t)\}}{\{|\boldsymbol{X}(s_0, t) - \boldsymbol{X}(s, t)|^2 + \mu^2\}^{\frac{3}{2}}} - \left(\frac{\partial \boldsymbol{X}}{\partial s}\right)_0 \wedge \left(\frac{\partial^2 \boldsymbol{X}}{\partial s^2}\right) \bar{P}(s, t) \right] \mathrm{d}s$$

$$+ \frac{1}{2} \left(\frac{\partial \boldsymbol{X}}{\partial s}\right)_0 \wedge \left(\frac{\partial^2 \boldsymbol{X}}{\partial s^2}\right)_0 \int_{-1}^{1} \bar{P}(s, t)\, \mathrm{d}s - \frac{1}{2} \int_{-1}^{1} \left[\frac{\partial \boldsymbol{X}}{\partial s} \wedge \frac{\boldsymbol{X}(s_0, t) - \boldsymbol{X}(s, t)}{|\boldsymbol{X}(s_0, t) - \boldsymbol{X}(s, t)|^3} \right]_{\text{image}} \mathrm{d}s. \tag{5}$$

Here the notation 'image' in the last integral indicates that the integration is performed on the image vortex loop (figure 1). A vector $\boldsymbol{X}_{\text{image}}(s, t)$ to a point on the

Case	1	2	3
sgn (Γ)	+	+	−
Direction of motion	Down	Down	Up
Angle of attack, α	60	80	70
Initial ring radius, R	1	1	1
Initial core radius, a_0	0.05	0.05	0.05
Initial distance from the wall, l	1.25	0.75	1.44

TABLE 1. Parameters associated with the vortex trajectories

image is obtained by changing the sign of the y-component of the vector $\boldsymbol{X}(s,t)$ to a point on the vortex. The function $\bar{P}$ in (5) is defined by

$$\bar{P}(s,t) = \frac{\frac{1}{2}(s-s_0)^2}{\left\{(s-s_0)^2\left|\frac{\partial \boldsymbol{X}}{\partial s}\right|^2_{s-s_0} + \mu^2\right\}^{\frac{3}{2}}}, \tag{6}$$

and is introduced in (5) following a procedure due to Moore (1972). The integrand in (1) is rapidly varying near $s = s_0$ for small a (and hence μ); adding and subtracting the leading-order term of the integrand yields the first integral in (5) of a function which is $O(1)$ everywhere. The second integral in (5) may be evaluated analytically.

Calculations were carried out for the three cases listed in table 1, where the parameters associated with the initial vortex configurations are given. The solution of (5) was advanced for each node using a fourth-order Runge–Kutta method; the derivatives in the integrands were evaluated using central-difference formulae and the integrations along the vortex were carried out using Simpson's rule. At any stage in the integrations, the current value of the core radius was evaluated using (3).

It was observed in the numerical work that the integrations tended to become unstable unless very small time steps were used; in addition, the stability problem was exacerbated as the number of nodal points on the vortex was increased to ensure a better spatial resolution. The reason is associated with the relatively small initial values of a_0 that were used here as opposed to previous studies (Dhanak & De Bernardinis 1981; Dhanak 1981) where the values of a were typically almost an order of magnitude larger. The use of thick vortex cores brings into question the validity of using the thin-filament approximation on which (5) is based; in the present study, thick cores were considered undesirable since situations where the vortex makes a close approach to the wall are of interest. It may be inferred from (5) that near the point s_0 the denominator in the first integral is $O(a^3)$ which tends to emphasize numerical errors in the approximation to $\partial \boldsymbol{X}/\partial s$. The variation near $s = s_0$ becomes more severe as a is decreased and using relatively large time steps results in strong instability of the numerical scheme. In the present study, a small time step of $\Delta t = 0.001$ was used throughout the calculations.

The trajectory for case 1 is depicted in figure 3 where the dimensionless time interval between vortex locations is 0.1. In this case the circulation Γ is positive and the initial angle of attack is $\alpha = 60°$. As the ring moves towards the wall it distorts into a loop. Vortex stretching plays an increasingly important role as the vortex approaches the wall; as the loop stretches, the core radius decreases and during the sequence in figure 3, the core radius decreased from 0.05 to 0.0462.

Once a vortex trajectory has been computed, the position of the vortex loop is known as a function of time and, at any instant, the inviscid velocity distribution

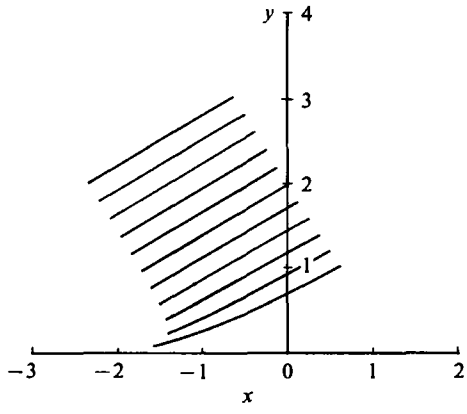

(*a*) Side view

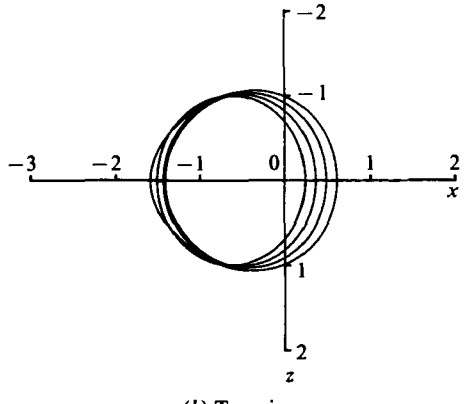

(*b*) Top view

FIGURE 3. Temporal development of a vortex loop moving towards the wall for case 1; the initial angle of attack $\alpha = 60°$.

near the wall induced by the moving vortex may be computed from the Biot–Savart law. In particular, the dimensionless velocity field at any point in the half-space $y > 0$ and not on the vortex is given by

$$\boldsymbol{u}(\boldsymbol{X}_0, t) = \tfrac{1}{2}\,\mathrm{sgn}\,(\Gamma)\left\{\int_{-1}^{1} \frac{\partial \boldsymbol{X}_\mathrm{L}}{\partial s} \wedge \frac{(\boldsymbol{X}_0 - \boldsymbol{X}_\mathrm{L}(s,t))}{|\boldsymbol{X}_0 - \boldsymbol{X}_\mathrm{L}(s,t)|^3}\,\mathrm{d}s - \int_{-1}^{1} \frac{\partial \boldsymbol{X}_\mathrm{I}}{\partial s} \wedge \frac{(\boldsymbol{X}_0 - \boldsymbol{X}_\mathrm{I}(s,t))}{|\boldsymbol{X}_0 - \boldsymbol{X}_\mathrm{I}(s,t)|^3}\,\mathrm{d}s\right\}. \quad (7)$$

Here the vectors

$$\boldsymbol{X}_\mathrm{L} = x_\mathrm{L}\hat{\boldsymbol{i}} + y_\mathrm{L}\hat{\boldsymbol{j}} + z_\mathrm{L}\hat{\boldsymbol{k}}, \quad \boldsymbol{X}_\mathrm{I} = x_\mathrm{L}\hat{\boldsymbol{i}} - y_\mathrm{L}\hat{\boldsymbol{j}} + z_\mathrm{L}\hat{\boldsymbol{k}}, \quad (8)$$

are used to denote the position of an arbitrary point on the vortex loop and its image respectively. The vectors $\hat{\boldsymbol{i}}$, $\hat{\boldsymbol{j}}$ and $\hat{\boldsymbol{k}}$ are unit vectors in the x, y and z directions respectively. Now consider the form of (7) as $y \to 0$ for which the inviscid velocity at the wall becomes

$$\boldsymbol{u}(\boldsymbol{X}_\mathrm{w}) = U_\mathrm{w}(x, z, t)\,\hat{\boldsymbol{i}} + W_\mathrm{w}(x, z, t)\,\hat{\boldsymbol{k}}, \quad (9)$$

where
$$U_w(x,z,t) = \operatorname{sgn}(\Gamma)\int_{-1}^{1} \frac{\left[(z-z_L)\frac{\partial y_L}{\partial s} + y_L\frac{\partial z_L}{\partial s}\right]}{\{(x-x_L)^2+y_L^2+(z-z_L)^2\}^{\frac{3}{2}}}\mathrm{d}s, \tag{10}$$

$$W_w(x,z,t) = -\operatorname{sgn}(\Gamma)\int_{-1}^{1} \frac{\left[y_L\frac{\partial x_L}{\partial s} + (x-x_L)\frac{\partial y_L}{\partial s}\right]}{\{(x-x_L)^2+y_L^2+(z-z_L)^2\}^{\frac{3}{2}}}\mathrm{d}s. \tag{11}$$

In this study, the boundary-layer development on the symmetry plane $z = 0$ is of interest and thus it is necessary to evaluate the special forms of (10) and (11) as $z \to 0$. It is evident that x_L, y_L and $\partial z_L/\partial s$ are symmetric about $z = 0$ while $\partial x_L/\partial s$, $\partial y_L/\partial s$ and z_L are antisymmetric. On the symmetry plane, a dimensionless streamwise velocity is defined according to

$$U_\infty = \lim_{z\to 0} U_w(x,z,t), \tag{12}$$

and it may readily be shown that

$$U_\infty(x,t) = 2\operatorname{sgn}(\Gamma)\int_0^1 \frac{\left[y_L\frac{\partial z_L}{\partial s} - z_L\frac{\partial y_L}{\partial s}\right]}{\{(x-x_L)^2+y_L+z_L^2\}^{\frac{3}{2}}}\mathrm{d}s. \tag{13}$$

The spanwise velocity W_w vanishes as $z \to 0$ but the gradient $\partial W_w/\partial z$ is non-zero and near $z = 0$, W_w may be written

$$W_w(x,z,t) \sim z\theta_\infty(x,t) + \ldots \quad \text{as } z \to 0. \tag{14}$$

It is then easily shown that

$$\theta_\infty(x,t) = -6\operatorname{sgn}(\Gamma)\int_0^1 \frac{z_L\left[y_L\frac{\partial x_L}{\partial s} + (x-x_L)\frac{\partial y_L}{\partial s}\right]}{\{(x-x_L)^2+y_L^2+z_L^2\}^{\frac{5}{2}}}\mathrm{d}s. \tag{15}$$

At any stage in the vortex motion, values of $x_L(s,t)$, $y_L(s,t)$ and $z_L(s,t)$ define the current location of the vortex and are known from the numerical solution of (5). A numerical integration of (14) and (15) is then readily carried out to evaluate U_∞ and θ_∞; this is the information required to solve the boundary-layer problem on the symmetry plane.

3. Boundary-layer formulation

Dimensionless variables for the boundary-layer flow induced by the moving vortex may be defined in terms of the initial ring radius R and a speed $|\kappa|/R$, where $\kappa = \Gamma/2\pi$ is the constant strength of the vortex. Let

$$\tilde{y} = \frac{y^* Re^{\frac{1}{2}}}{R}, \quad v = \frac{Re^{\frac{1}{2}} R v^*}{|\kappa|}, \tag{16}$$

be the scaled normal coordinate and velocity respectively, where $Re = |\kappa|/\nu$ is the

Reynolds number and ν is the kinematic viscosity. The three-dimensional boundary-layer equations in these variables are

$$\frac{\partial u}{\partial t}+u\frac{\partial u}{\partial x}+v\frac{\partial u}{\partial \tilde{y}}+w\frac{\partial u}{\partial z}=-\frac{\partial p_\infty}{\partial x}+\frac{\partial^2 u}{\partial \tilde{y}^2}, \tag{17}$$

$$\frac{\partial w}{\partial t}+u\frac{\partial w}{\partial x}+v\frac{\partial w}{\partial \tilde{y}}+w\frac{\partial w}{\partial z}=-\frac{\partial p_\infty}{\partial z}+\frac{\partial^2 w}{\partial \tilde{y}^2}, \tag{18}$$

$$\frac{\partial u}{\partial x}+\frac{\partial v}{\partial \tilde{y}}+\frac{\partial w}{\partial z}=0. \tag{19}$$

Here $p_\infty(x, z, t)$ is the pressure distribution due to the moving vortex evaluated at the edge of the boundary layer. The calculation of the entire boundary-layer flow field is a difficult numerical task because a very large number of mesh points would be required to yield an accurate description of the unsteady three-dimensional flow. In the present situation however, it is possible to calculate the boundary-layer development on the symmetry plane $z = 0$ and to obtain a limited amount of three-dimensional information there. Near the symmetry plane, the u- and w-velocity components and pressure may be written

$$u = u(x, \tilde{y}, t)+O(z^2), \quad w = z\theta(x, \tilde{y}, t)+O(z^3), \tag{20a, b}$$

where

$$\theta(x, \tilde{y}, t) = \left.\frac{\partial w}{\partial z}\right|_{z=0}, \tag{21}$$

the form of which is compatible with the inviscid velocity distributions at the boundary-layer edge; the first terms represent the leading-order representation of the solution for small z and the order of the first terms neglected is indicated in (20).

Substituting (20) into (17)–(19) and taking the limit $z \to 0$ leads to

$$\frac{\partial u}{\partial t}+u\frac{\partial u}{\partial x}+v\frac{\partial u}{\partial \tilde{y}}=\frac{\partial U_\infty}{\partial t}+U_\infty\frac{\partial U_\infty}{\partial x}+\frac{\partial^2 u}{\partial \tilde{y}^2}, \tag{22}$$

$$\frac{\partial \theta}{\partial t}+u\frac{\partial \theta}{\partial x}+v\frac{\partial \theta}{\partial \tilde{y}}+\theta^2=\frac{\partial \theta_\infty}{\partial t}+U_\infty\frac{\partial \theta_\infty}{\partial x}+\theta_\infty^2+\frac{\partial^2 \theta}{\partial \tilde{y}^2}, \tag{23}$$

$$\frac{\partial u}{\partial x}+\frac{\partial v}{\partial \tilde{y}}+\theta=0. \tag{24}$$

This set of equations defines the unsteady boundary-layer problem on the symmetry plane $z = 0$ with the boundary conditions,

$$\begin{aligned} u = v = \theta = 0 \quad &\text{at } \tilde{y} = 0, \\ u \to U_\infty, \quad \theta \to \theta_\infty \quad &\text{as } \tilde{y} \to \infty, \end{aligned} \tag{25}$$

where U_∞ and θ_∞ are given by (13) and (15).

In order to motivate the subsequent transformations, it is worthwhile to consider the general nature of typical distributions of $\theta_\infty(x, t)$ and $U_\infty(x, t)$ which are plotted in figure 4 for case 2 at $t = 0.15$ as an example. It may be seen from figure 4 that U_∞ changes sign, being predominantly negative to the left of the origin and positive to the right. In addition to the one zero of U_∞, which is evident in figure 4, there is another zero for large negative x. It can be inferred from (13) that the second zero will always occur; the denominator in the integrand of (13) is quadratic in x and

hence as $x \to +\infty$ or $x \to -\infty$, $U_\infty(x,t)$ must be of the same sign. The fact that $U_\infty(x,t)$ has two zeros whose positions change with time precludes writing the boundary-layer solution in the form $u = U_\infty(x,t)F(x,y,t)$, which is normally a convenient form for computational purposes. Consequently, a decomposition of U_∞ was sought of the form

$$U_\infty(x,t) = U_1(x,t) + U_2(x,t), \tag{26}$$

where U_1 and U_2 are to be selected so that neither function has a zero for all t and in addition U_1 is of the opposite sign to U_2. This decomposition could be carried out in a variety of ways and one convenient choice is

$$\left.\begin{aligned} U_1(x,t) &= -2\,\mathrm{sgn}\,(\Gamma)\int_0^1 \frac{z_L \dfrac{\partial y_L}{\partial s}}{\{(x-x_L)^2+y_L^2+z_L^2\}^{\frac{3}{2}}}\,\mathrm{d}s \\ &\quad +2\,\mathrm{sgn}\,(\Gamma)\int_0^{0.5} \frac{y_L \dfrac{\partial z_L}{\partial s}}{\{(x-x_L)^2+y_L^2+z_L^2\}^{\frac{3}{2}}}\,\mathrm{d}s, \\ U_2(x,t) &= 2\,\mathrm{sgn}\,(\Gamma)\int_{0.5}^1 \frac{y_L \dfrac{\partial z_L}{\partial s}}{\{(x-x_L)^2+y_L^2+z_L^2\}^{\frac{3}{2}}}\,\mathrm{d}s. \end{aligned}\right\} \tag{27}$$

It may readily be verified that U_1 and U_2 have different signs for all x.

It may be seen from figure 4 that for Γ positive, θ_∞ is predominantly positive since the spanwise inviscid velocity is primarily directed away from the symmetry plane $z = 0$ as the vortex loop moves towards the wall. However it may be inferred from (15) that θ_∞ has opposite signs as $x \to \pm\infty$ and thus there must be at least one zero of θ_∞ at some x-location; the zero in θ_∞ occurs in figure 4 for $x < 0$. Thus for x sufficiently negative (for positive Γ) there is a region where the inviscid spanwise flow is towards the symmetry plane. For Γ negative, the vortex recedes from the wall and the direction of the spanwise inviscid velocity is reversed. A decomposition of θ_∞ was carried out according to

$$\theta_\infty(x,t) = \theta_1(x,t) + \theta_2(x,t), \tag{28}$$

where θ_1 and θ_2 were selected so that neither function has a zero and each is of opposite sign. Again there is a variety of ways in which this decomposition can be carried out; a convenient choice (Ersoy & Walker 1985*b*) is

$$\left.\begin{aligned} \theta_1(x,t) &= +3\,\mathrm{sgn}\,(\Gamma)\int_0^1 \frac{(x-x_L-0.5)^2}{\{(x-x_L)^2+y_L^2+z_L^2\}^{\frac{5}{2}}} z_L \frac{\partial y_L}{\partial s}\,\mathrm{d}s, \\ \theta_2(x,t) &= -3\,\mathrm{sgn}\,(\Gamma)\int_0^1 \frac{(x-x_L+0.5)^2}{\{(x-x_L)^2+y_L^2+z_L^2\}^{\frac{5}{2}}} z_L \frac{\partial y_L}{\partial s}\,\mathrm{d}s \\ &\quad -6\,\mathrm{sgn}\,(\Gamma)\int_0^1 \frac{z_L y_L \dfrac{\partial y_L}{\partial s}}{\{(x-x_L)^2+y_L^2+z_L^2\}^{\frac{5}{2}}}\,\mathrm{d}s. \end{aligned}\right\} \tag{29}$$

The decompositions of U_∞ and θ_∞ are also plotted in figure 4. Note that the vortex is closest to the wall for $x < 0$ and here U_2 and θ_2 show a relatively large pulse.

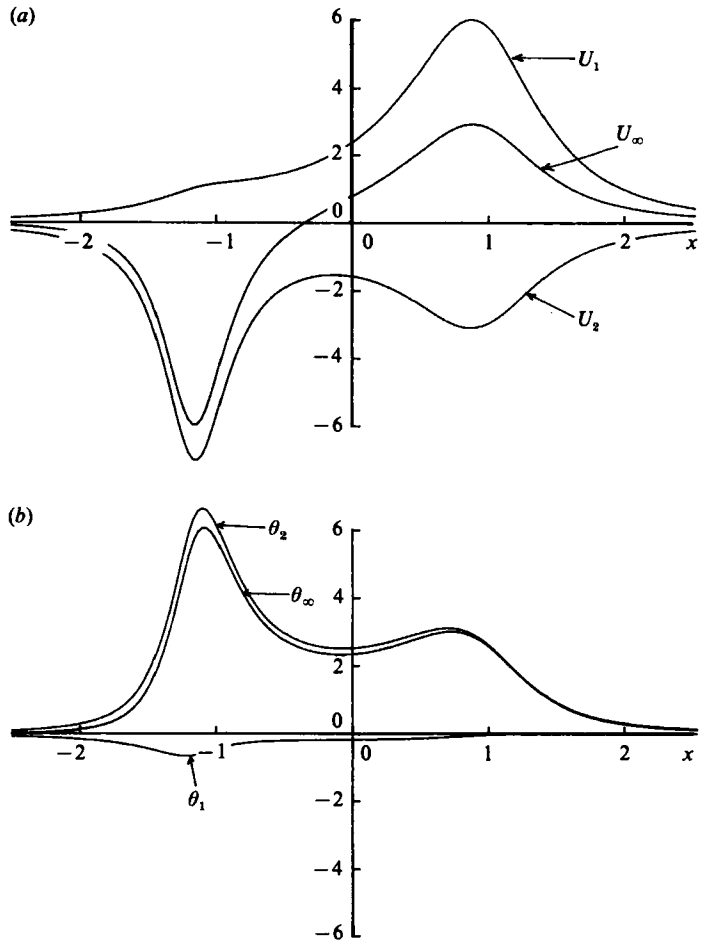

FIGURE 4. Typical distributions of U_1 and U_2, the decomposition of U_∞ and θ_1 and θ_2, the decomposition of θ_∞ (case 2 at $t = 0.15$).

Returning now to the boundary-layer equations on the symmetry plane, it is convenient to introduce a function $\phi(x, y, t)$ defined by

$$\theta = \frac{\partial \phi}{\partial \tilde{y}}, \quad \phi(x, 0, t) = 0, \tag{30}$$

and another function $\psi(x, y, t)$ which is defined in terms of the velocity components u and v by

$$u = \frac{\partial \psi}{\partial \tilde{y}}, \quad v = -\frac{\partial \psi}{\partial x} - \phi, \quad \psi(x, 0, t) = 0. \tag{31}$$

It may be verified that the continuity equation (24) on the symmetry plane $z = 0$ is identically satisfied.

The doubly infinite range of the streamwise coordinate x may be transformed to a finite range by defining a new streamwise variable ξ according to

$$\xi = \frac{2}{\pi} \arctan\left\{\frac{2x - x_1 - x_2}{x_1 - x_2}\right\}. \tag{32}$$

Here x_1 and x_2 correspond to the streamwise locations where the vortex loop intersects the symmetry plane. The transformation is one-to-one and maps the range $(-\infty, \infty)$ of x to the finite range $(-1, 1)$ in ξ. Note that at any stage in a numerical solution of the vortex loop trajectory, values of x_1 and x_2 are readily available corresponding to the x-components of the solution of (5) at $s = 0$ and $s = 1$ respectively. An important advantage of the ξ-coordinate is that the leading and trailing slices of the vortex loop at x_1 and x_2 correspond to $\xi = \pm\frac{1}{2}$ respectively for all t; thus although the leading and trailing portions of the vortex loop may exhibit substantial movement in the x-coordinate, they are frozen in the ξ-coordinate.

The motion is assumed to initiate when the vortex is first introduced in the flow; this initial condition is a reasonable simulation of experimental studies where a vortex ring is created abruptly with a piston generator (Falco 1983; Walker *et al.* 1987). Immediately a thin boundary layer of thickness $O(t^{\frac{1}{2}})$ begins to develop on the wall and to take this behaviour into account, it is convenient to define a scaled normal coordinate according to

$$\eta = \frac{y}{2t^{\frac{1}{2}}}, \tag{33}$$

and to define the streamwise velocity and spanwise shear θ by

$$\frac{\partial \psi}{\partial \tilde{y}} = 2U_1 \operatorname{erf}\eta + (U_2 - U_1)\frac{\partial \Psi}{\partial \eta}, \quad \frac{\partial \phi}{\partial \tilde{y}} = \theta_1 \operatorname{erf}\eta + \theta_2 \frac{\partial \Phi}{\partial \eta}. \tag{34}$$

Here Ψ and Φ are related to the original variables ψ and ϕ by

$$\psi = 2t^{\frac{1}{2}}\{2U_1 I(\eta) + (U_2 - U_1)\Psi\}, \quad \phi = 2t^{\frac{1}{2}}\{\theta_1 I(\eta) + \theta_2 \Phi\}, \tag{35}$$

where

$$I(\eta) = \eta \operatorname{erf}\eta + \frac{e^{-\eta^2}}{\pi^{\frac{1}{2}}} - \frac{1}{\pi^{\frac{1}{2}}}. \tag{36}$$

The v-component may be obtained from the second of (31) and

$$v = -2t^{\frac{1}{2}}\left\{\theta_1 I(\eta) + \theta_2 \Phi + 2\frac{\partial \xi}{\partial x}\frac{\partial U_1}{\partial \xi} I(\eta) + \frac{\partial \xi}{\partial x}\left\{\frac{\partial U_2}{\partial \xi} - \frac{\partial U_1}{\partial \xi}\right\}\Psi + (U_2 - U_1)\frac{\partial \xi}{\partial x}\frac{\partial \Psi}{\partial \xi}\right\}. \tag{37}$$

The boundary conditions associated with Ψ and Φ are

$$\Psi = \frac{\partial \Psi}{\partial \eta} = \Phi = \frac{\partial \Phi}{\partial \eta} = 0 \quad \text{at } \eta = 0, \quad \lim_{\eta \to \infty} \frac{\partial \Psi}{\partial \eta} = \lim_{\eta \to \infty} \frac{\partial \Phi}{\partial \eta} = 1, \tag{38}$$

for all ξ and t.

The principal motivation for writing the velocity components in form of (34) is associated with the numerical solution procedure. It is convenient (for a variety of reasons) to deal with a dependent variable which varies from 0 to 1 across the boundary layer; (34) defines such dependent variables $\partial\Psi/\partial\eta$ and $\partial\Phi/\partial\eta$ but the transformations are by no means unique. The main factors which motivate the selected form of (34) are: (i) the coefficients of $\partial\Psi/\partial\eta$ and $\partial\Phi/\partial\eta$ in (34) cannot vanish at any x in the range $-\infty < x < \infty$ for all t and (ii) the coefficients of $\partial\Psi/\partial\eta$ and $\partial\Phi/\partial\eta$ should contain a dominant portion of the inviscid velocity distribution (otherwise it emerges that the convergence rate of the numerical scheme is adversely impacted). Portions of the inviscid velocity distributions in (34) are associated with the error function. Note that the error function will emerge to be a solution of boundary-layer equations at $t = 0$ but in the context of (34) should be viewed simply as a convenient function which varies from 0 to 1 across the boundary layer. In view

of the distributions of θ_1 and θ_2 depicted in figure 4, the choice of the decomposition for θ in (34) was relatively straightforward. Different forms for the decomposition of u were considered (see Ersoy & Walker 1985*b*) and it was determined that the form given by (34) was satisfactory in all cases.

Both momentum equations (22) and (23) assume a similar form; the x-momentum equation (22) becomes

$$4t\frac{\partial U}{\partial t}=\frac{\partial^2 U}{\partial \eta^2}+P\frac{\partial U}{\partial \eta}+R_x U+Q\frac{\partial U}{\partial \xi}+G_x, \quad U=\frac{\partial \Psi}{\partial \eta}, \tag{39}$$

where the x subscript denotes functions associated only with the x-momentum equation and

$$\left.\begin{aligned}
P &= 2\eta+4tV,\\
R_x &= -\frac{4t}{U_2-U_1}\Bigg[\frac{\partial U_2}{\partial t}-\frac{\partial U_1}{\partial t}+2(U_2-U_1)\frac{\partial \xi}{\partial x}\frac{\partial U_1}{\partial \xi}\operatorname{erf}\eta\\
&\quad+\left\{\frac{\partial U_2}{\partial \xi}-\frac{\partial U_1}{\partial \xi}\right\}\left\{\frac{\partial \xi}{\partial t}+2U_1\frac{\partial \xi}{\partial x}\operatorname{erf}\eta+(U_2-U_1)\frac{\partial \xi}{\partial x}U\right\}\Bigg],\\
Q &= -4t\left[\frac{\partial \xi}{\partial t}+\frac{\partial \xi}{\partial x}\{2U_1\operatorname{erf}\eta+(U_2-U_1)U\}\right],\\
G_x &= -\frac{4t}{U_2-U_1}\Bigg[-\frac{\partial U_1}{\partial t}-\frac{\partial U_2}{\partial t}-\left(\frac{\partial U_1}{\partial \xi}+\frac{\partial U_2}{\partial \xi}\right)\left(\frac{\partial \xi}{\partial t}+(U_1+U_2)\frac{\partial \xi}{\partial x}\right)\\
&\quad+2\frac{\partial U_1}{\partial t}\operatorname{erf}\eta+2\frac{\partial U_1}{\partial \xi}\frac{\partial \xi}{\partial t}\operatorname{erf}\eta+4U_1\frac{\partial U_1}{\partial \xi}\frac{\partial \xi}{\partial x}\operatorname{erf}^2\eta-\frac{4U_1}{\pi^{\frac{1}{2}}}\mathrm{e}^{-\eta^2}V\Bigg].
\end{aligned}\right\} \tag{40}$$

In these equations, the quantity V is defined from (37) by

$$V=\theta_1 I(\eta)+\theta_2\Phi+2\frac{\partial \xi}{\partial x}\frac{\partial U_1}{\partial \xi}I(\eta)+\left(\frac{\partial U_2}{\partial \xi}-\frac{\partial U_1}{\partial \xi}\right)\frac{\partial \xi}{\partial x}\Psi+(U_2-U_1)\frac{\partial \xi}{\partial x}\frac{\partial \Psi}{\partial \xi}, \tag{41}$$

and $I(\eta)$ is given by (36). The z-momentum equation (23) becomes

$$4t\frac{\partial \Upsilon}{\partial t}=\frac{\partial^2 \Upsilon}{\partial \eta^2}+P\frac{\partial \Upsilon}{\partial \eta}+R_z\Upsilon+Q\frac{\partial \Upsilon}{\partial \xi}+G_z, \quad \Upsilon=\frac{\partial \Phi}{\partial \eta}, \tag{42}$$

where the subscript z denotes functions associated only with the z-momentum equation and

$$\left.\begin{aligned}
R_z &= -\Bigg[4t\frac{1}{\theta_2}\left(\frac{\partial \theta_2}{\partial t}+\frac{\partial \xi}{\partial t}\frac{\partial \theta_2}{\partial \xi}\right)+\frac{2U_1}{\theta_2}\frac{\partial \xi}{\partial x}\frac{\partial \theta_2}{\partial \xi}\operatorname{erf}\eta\\
&\quad+\frac{(U_2-U_1)}{\theta_2}\frac{\partial \xi}{\partial x}\frac{\partial \theta_2}{\partial \xi}U+2\theta_1\operatorname{erf}\eta+\theta_2\Upsilon\Bigg],\\
G_z &= -\frac{4t}{\theta_2}\Bigg[-\frac{\partial \theta_1}{\partial t}-\frac{\partial \theta_2}{\partial t}-\left(\frac{\partial \theta_1}{\partial \xi}+\frac{\partial \theta_2}{\partial \xi}\right)\left(\frac{\partial \xi}{\partial t}+(U_1+U_2)\frac{\partial \xi}{\partial x}\right)\\
&\quad-(\theta_1+\theta_2)^2+\left(\frac{\partial \theta_1}{\partial t}+\frac{\partial \xi}{\partial t}\frac{\partial \theta_1}{\partial \xi}\right)\operatorname{erf}\eta+2U_1\frac{\partial \xi}{\partial x}\frac{\partial \theta_1}{\partial \xi}\operatorname{erf}^2\eta\\
&\quad+(U_2-U_1)\frac{\partial \xi}{\partial x}\frac{\partial \theta_1}{\partial \xi}U\operatorname{erf}\eta-\frac{2}{\pi^{\frac{1}{2}}}V\theta_1\mathrm{e}^{-\eta^2}+\theta_1^2\operatorname{erf}^2\eta\Bigg],
\end{aligned}\right\} \tag{43}$$

where V is given by (41).

In both sets of equations (39) and (42), θ_1, θ_2, U_1 and U_2 appear, as well as derivatives of these quantities with respect to ξ and t; these quantities are known functions of ξ and t which are evaluated from the computed vortex trajectory through (27) and (29). In addition, the gradients $\partial\xi/\partial x$ and $\partial\xi/\partial t$ may be evaluated by differentiating the transformation (32); at any stage, values of $x_1(t)$ and $x_2(t)$ are known from the trajectory information and $\mathrm{d}x_1/\mathrm{d}t$ and $\mathrm{d}x_2/\mathrm{d}t$ may be computed from (5) by taking $s = 0$ and $s = 1$ respectively. Note that both (39) and (42) are nonlinear since the functional coefficients contain the dependent variables U, Υ, Ψ and Φ. Finally the associated boundary conditions are

$$u = \Psi = \Upsilon = \Phi = 0 \quad \text{at } \eta = 0, \quad U, \Upsilon \to 1 \quad \text{as } \eta \to \infty. \tag{44}$$

4. The boundary-layer equations at infinity

The solution of the boundary-layer equations (39) and (42) as $|x| \to \infty$ ($\xi \to \pm 1$) develops independently of the solution in the interior ($-1 < \xi < 1$). It may be seen from (27) and (29) that U_1, U_2, θ_1 and θ_2 are all $O(x^{-3})$ as $|x| \to \infty$; in addition it is easily verified that $\partial\xi/\partial x = O(x^{-2})$ and $\partial\xi/\partial t = O(x^{-1})$ as $|x| \to \infty$. Consequently it is easily shown that the limiting forms of (39) and (42) are

$$4t\frac{\partial \bar{U}}{\partial t} = \frac{\partial^2 \bar{U}}{\partial \eta^2} + 2\eta\frac{\partial \bar{U}}{\partial \eta} - 4tA_1(t)\,\bar{U} - 4t\{A_2(t)(\operatorname{erf}\eta - 1) - A_1(t)\}, \tag{45}$$

$$4t\frac{\partial \bar{\Upsilon}}{\partial t} = \frac{\partial^2 \bar{\Upsilon}}{\partial \eta^2} + 2\eta\frac{\partial \bar{\Upsilon}}{\partial \eta} - 4tB_1(t)\,\bar{\Upsilon} + 4tB_1(t)\operatorname{erf}\eta, \tag{46}$$

as $|\xi| \to 1$. Here $\bar{U}(\eta, t)$, $\bar{\Upsilon}(h, t)$ denote the limiting values of $U(\xi, \eta, t)$ and $\Upsilon(\xi, \eta, t)$ as $|\xi| \to \infty$ and the coefficients in (45) and (46) are given by

$$A_1(t) = \frac{1}{(\alpha_2 - \alpha_1)}\frac{\mathrm{d}}{\mathrm{d}t}(\alpha_2 - \alpha_1), \quad A_2(t) = \frac{2}{(\alpha_2 - \alpha_1)}\frac{\mathrm{d}\alpha_1}{\mathrm{d}t}, \tag{47}$$

$$B_1(t) = \frac{1}{\beta_1}\frac{\mathrm{d}\beta_1}{\mathrm{d}t}, \tag{48}$$

where

$$\alpha_1(t) = \int_0^1 z_{\mathrm{L}}\frac{\partial y_{\mathrm{L}}}{\partial s}\,\mathrm{d}s - \int_0^{0.5} y_{\mathrm{L}}\frac{\partial z_{\mathrm{L}}}{\partial s}\,\mathrm{d}s, \tag{49}$$

$$\alpha_2(t) = -\int_{0.5}^1 y_{\mathrm{L}}\frac{\partial z_{\mathrm{L}}}{\partial s}\,\mathrm{d}s, \tag{50}$$

$$\beta_1(t) = \int_0^1 z_{\mathrm{L}}\frac{\partial y_{\mathrm{L}}}{\partial s}\,\mathrm{d}s. \tag{51}$$

At any stage in the integrations, the time-dependent coefficients in (45) and (46) may be evaluated from the trajectory information. The boundary conditions for $\bar{U}$ and $\bar{\Upsilon}$ are also given by 44).

5. The numerical solution

In order to initiate a boundary-layer integration, it is necessary to specify an initial boundary-layer state, and in the present study the boundary-layer flow was assumed to develop abruptly from rest upon insertion of the vortex ring into the

stagnant flow above the wall. The solution for U, Υ and $\bar{U}$, $\bar{\Upsilon}$ which satisfies the limiting forms of (39), (42), (45) and (46) respectively as $t \to 0^+$ is given by

$$U = \bar{U} = \Upsilon = \bar{\Upsilon} = \operatorname{erf}\eta. \tag{52}$$

The boundary-layer solutions evolve forward in time from this initial state.

The numerical method used is similar to that described by Walker (1978) and Doligalski & Walker (1984) and will not be discussed in detail here; the scheme is an implicit method which is second-order accurate in both space directions and in time. A rectangular mesh in the (ξ, η)-plane was defined with uniform mesh spacings of h_1 in the ξ-direction and h_2 in the η-direction; a number of mesh sizes were considered as a check on the accuracy and values of $h_1 = 0.01$ and $h_2 = 0.05$ were determined to be sufficiently small to obtain reliable results. The last of conditions (44) were enforced at an outer boundary of $\eta_\infty = 6$ as an approximation; this value of η_∞ was determined to be sufficiently large to ensure that no significant changes in the solution would occur for larger η_∞. A constant time step of $\Delta t = 0.001$ was used to advance the boundary-layer solution forward in time corresponding to the time step used to compute the trajectory of the vortex loop as described in §2.

The solution for U and Υ was advanced from time step to time step using the following general procedure. First the solutions of (45) and (46) were advanced one time step using a conventional Crank–Nicholson procedure (see for example Ersoy & Walker 1985*b*); once the solutions for $\bar{U}$ and $\bar{\Upsilon}$ are determined in the current time plane, the solution at $\xi = \pm 1$ is known and the solution for the interior problem $-1 < \xi < 1$ and $0 < \eta < \eta_\infty$ can be advanced into the current time plane. This was carried out using a method based on the Crank–Nicholson approach (Ersoy & Walker 1985*b*) with centred differences for the spatial derivatives; the difference equations associated with the approximations to (39) and (42) are nonlinear and at each time step, iteration is required. A Gauss–Seidel relaxation method was used to solve the difference equations and after each complete sweep of the mesh in the interior, the functional coefficients in (40) and (43) were updated using the current estimates of U and Υ; at any stage, estimates of Ψ and Φ were obtained from the current values of U and Υ using a numerical integration of the last of (39) and (42) based on Simpson's rule. The overall iteration was allowed to continue until convergence was obtained at a given time step; this was considered to have occurred when successive iterates for U and Υ differed by less than four significant figures at all internal mesh points. Typically 10–15 global iterations were required at each time step to achieve convergence; in the initial stages of the integrations, when rapid changes in the flow field take place, the scheme typically required on the order of 35–40 iterations. For the three cases which will be discussed here, calculations were carried out for on the order of 200–400 time steps.

6. Calculated results

In this section, calculated results for the three cases listed in table 1 will be described. The three-dimensional motion in the boundary layer is complex and in order to obtain a clear physical picture of the flow field, three types of streamline plots will be presented; these are: (*a*) instantaneous streamline plots in the symmetry plane (the (x, η)-plane); (*b*) instantaneous contours of constant θ in the (x, η)-plane; and (*c*) the instantaneous limiting streamlines on the wall (the (x, z)-plane) close to

the symmetry plane. In general, the equations of the streamlines in a three-dimensional flow are given by

$$\frac{\mathrm{d}x}{u} = \frac{\mathrm{d}\tilde{y}}{v} = \frac{\mathrm{d}z}{w} = \mathrm{d}\tau, \tag{53}$$

where τ is a variable measuring distance along a streamline. Since $w = 0$ on the symmetry plane, it may be inferred that once a fluid particle is located on the symmetry plane, it can only leave the plane at a stagnation point $u = v = 0$. Thus stagnation points in the symmetry plane are rather important features of the flow field. The streamlines were traced by numerical integration of (53) (Ersoy & Walker 1985*b*) using very small increments in τ.

The contours of constant θ show both the magnitude and direction of the spanwise flow near the symmetry plane; it follows from (20*b*) that constant-θ curves are lines of constant spanwise inflow or outflow at a fixed but small value of z. A third type of plot consisting of the instantaneous surface streamlines in the (x, z)-plane was found to be very useful in the interpretation of the motion. A limited amount of three-dimensional information is available from the present calculations; near the symmetry plane, u and w are given by (20). Near the wall, v is $O(y^2)$ while u and w are $O(y)$; thus for small y, the surface streamlines are given approximately by

$$\frac{\mathrm{d}z}{z\theta} = \frac{\mathrm{d}x}{u} \quad \text{for } \tilde{y} \ll 1, \tag{54}$$

near the symmetry plane ($z \ll 1$). In the limit as $y \to 0$, the equations of the surface streamlines become

$$\frac{\mathrm{d}z}{\mathrm{d}x} = z\frac{(\partial\theta/\partial\tilde{y})_{\tilde{y}=0}}{(\partial u/\partial\tilde{y})_{\tilde{y}=0}}. \tag{55}$$

In the present study, the limiting streamlines were plotted using (54) with the values of u and θ taken from the numerical solutions at the first mesh point from the wall ($\eta = h_2$). It is not possible to determine a specific maximum value of z for which the leading terms in (20) give an adequate representation; the maximum value of z used in the present plots was 0.1.

In the streamline plots, the instantaneous direction of flow is indicated with arrows; for the constant-θ curves, the magnitude and sign of each curve is shown to give an indication of the relative strength and magnitude of the spanwise flow near the symmetry plane. To give an indication of the current location of the vortex above the boundary layer as well as the timescale associated with the boundary-layer development, the initial streamwise location of the two points (x_1 and x_2) where the vortex loop intersects the symmetry plane are indicated by an open triangle at the top of each graph; the current streamwise positions of the extremities of the vortex loop $x_1(t)$ and $x_2(t)$ are marked by vertical arrows. Finally in order to present an undistorted view of the flow patterns, the plots are presented in terms of the dimensionless physical variable x rather than the streamwise coordinate ξ used in the numerical integrations. The subsequent plots of the developing boundary-layer flow represent a limited selection from the detailed sequences given by Ersoy & Walker (1985*b*).

In the first case considered here, the angle of approach of the initial vortex ring is $\alpha = 60°$ and the vortex moves towards the wall. The portion of the vortex which is closest to the wall dominates the flow development in the boundary layer and for this reason the plot window in the subsequent graphs is centred in the region $x < 0$ near

the current x_2. The streamlines in the symmetry plane at $t = 0.125$ are depicted in figure 5(*a*); there are two limiting streamlines in this plot which terminate on the wall at stagnation points labelled S1 and S2. The stagnation point S2 is characterized by flow away from the wall; in the interim between $t = 0$ and $t = 0.125$, as the vortex has moved closer to the wall, S2 has moved progressively to the right from $x = -2.8$ to about $x = -2.0$. On the other hand, S1 is characterized by flow towards the wall and has not moved significantly. A slight lifting of the streamlines near $x = -1.75$ may be observed in figure 5(*a*).

The constant-θ contours at $t = 0.125$ are shown in figure 5(*b*); the field is divided into two portions by the $\theta = 0$ line. To the right of this line, θ is positive and the spanwise flow is away from the symmetry plane; a maximum positive value of θ is achieved at about $x = -1.25$ starting on a line near $\eta = 2.0$ and extending outward through the boundary layer. To the left of the $\theta = 0$ line, all values of θ are negative but are smaller in absolute value than the positive values to the right of the $\theta = 0$ line; the region to the left of the $\theta = 0$ line is thus a region of relatively weak inflow towards the symmetry plane. In the early stages of the motion the contours of negative θ show a similar pattern to the contours of positive θ in figure 5(*b*). However as time increases a cusp forms in one of the negative-θ contours (Ersoy & Walker 1985*b*) and by $t = 0.125$ a new feature has developed in the form of an eye-shaped structure in the region of negative spanwise flow near the wall. At the centre of the eye, θ reaches an absolute minimum and thus the spanwise inflow achieves a maximum at the centre of the eye. The critical value of θ which encloses the eye is $\theta = -0.0557$ and it may be seen that the two tails of this curve ultimately rise vertically towards the inviscid-flow region.

The limiting surface streamlines at $t = 0.125$ are depicted in figure 5(*c*). These streamlines converge towards the stagnation point S2; θ is negative near S2 and, with reference to figure 5(*a*), it may be seen that near S2 the flow is towards the symmetry plane and away from the wall. Consequently S2 is a nodal point of separation (Lighthill 1963). Note that the surface streamlines to the right of S2 are evolving in a manner tending to approach the symmetry plane tangentially near $z = 0$ and almost perpendicular to the plane for larger values of z. The point S1 is a nodal point of attachment and here the flow is towards the wall and away from the symmetry plane. One feature of figure 5(*c*) and subsequent plots of the limiting streamline behaviour is worthy of note. The locus of points where $w = 0$ in the surface streamlines occurs on the limiting streamlines joining S1 to S2 where $\partial z/\partial x = 0$; there is one such locus of points in figure 5(*c*) and the point where this locus intersects the symmetry plane generally corresponds to the location where the $\theta = 0$ line intersects the wall. In figure 5(*b*, *c*) this occurs at about $x = -1.6$.

The next stage of development for case 1 is depicted in figure 6 at $t = 0.175$. It may be observed in figure 6(*a*) that the stagnation point S2 has shifted to near $x = -1.5$; furthermore a region of three-dimensional separation has developed to the left of S2 between the wall and the lifting streamlines in the upper portion of the boundary layer. The two new critical features in the streamline patterns in the symmetry plane are a new saddle-point stagnation point S3 as well as a focus which has been labelled F1. Note that this type of separation is rather different from the two-dimensional separations induced by vortex flows (Walker 1978; Doligalski & Walker 1984) in that the instantaneous streamlines do not form closed loops. In fact, the streamlines near the focus all spiral away from F1 which is in a region of negative θ and hence inflow towards the symmetry plane. Thus F1 is a stagnation point at which fluid particles are instantaneously entering the symmetry plane. All streamlines which spiral away

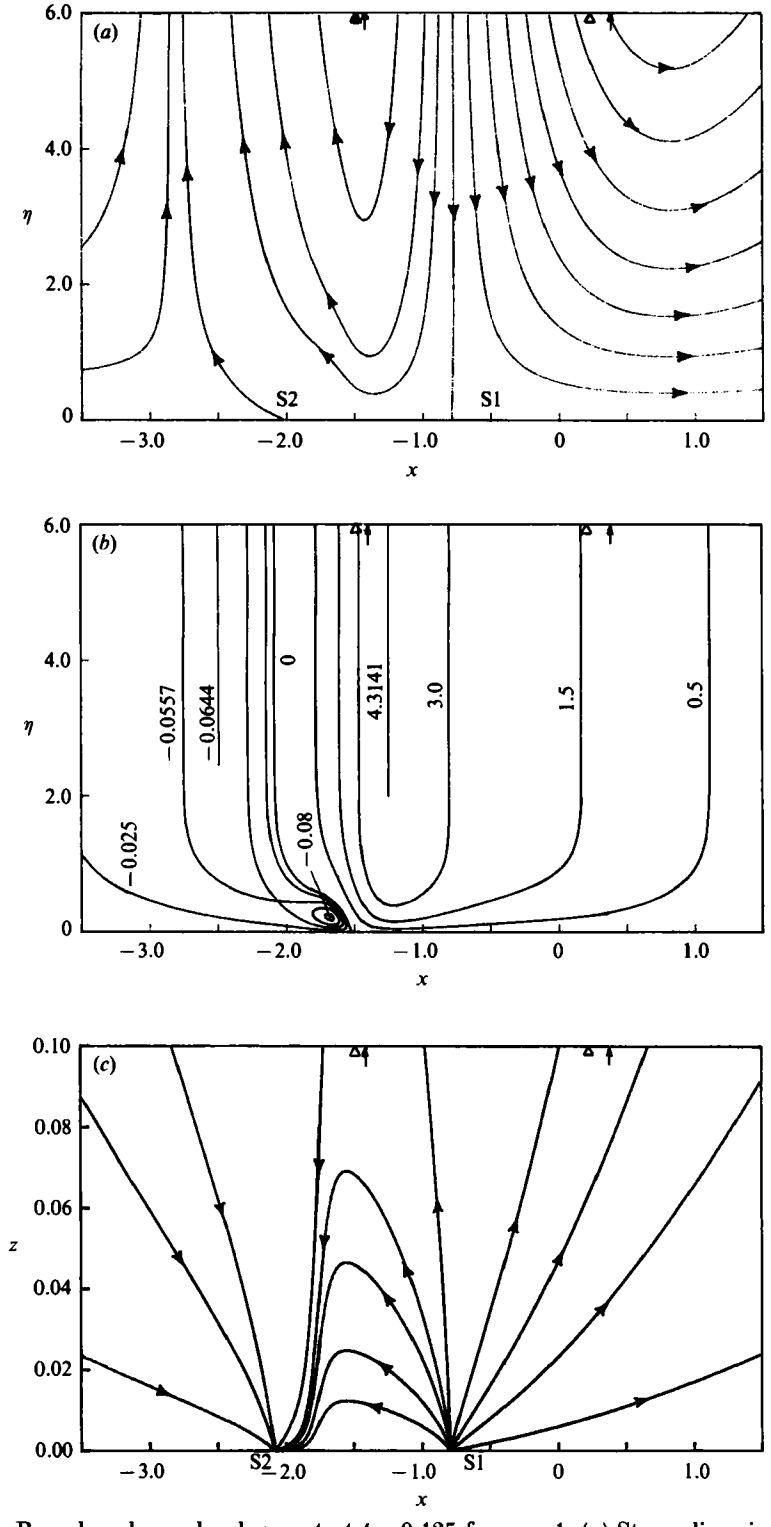

FIGURE 5. Boundary-layer development at $t = 0.125$ for case 1. (*a*) Streamlines in the symmetry plane; (*b*) constant-θ contours; (*c*) limiting surface streamlines in the (x, z)-plane.

from F1 trace a path towards the outer regions of the boundary layer in a corridor between the limiting streamlines through S2 and S3.

Lines of constant θ at $t = -0.175$ are depicted in figure 6(*b*) and it may be observed that the eye-shaped region, where the inflow to the symmetry plane reaches its maximum values, has increased in size. The critical curve $\theta = -0.0966$ enclosing this region now extends into the upper portion of the boundary layer as a single line. Note that the levels of inflow in the eye are increasing and that the location of the focus F1 is close to the centre of the 'eye'. In addition it may be observed that the variation on the right side of 'eye' is intensifying as evidenced by the relative closeness there of the constant-θ contours. The surface streamlines at $t = 0.175$ are plotted in figure 6(*c*) where it is evident that the streamlines from the stagnation point S1 now approach S2 in a rather striking way. Surface streamlines from either side of S2 now approach a limiting line which is perpendicular to the symmetry plane for small z.

A subsequent stage of development of the streamline patterns in the symmetry plane is shown in figure 7 at $t = 0.2$. The separation has grown in a direction normal to the wall; in addition, the streamline through S2 is approaching the vertical on the right side of the separation and the variation on the right side of the three-dimensional separation is becoming very intense. At this stage, the flow field near the right side of the separation is characterized by substantial boundary-layer growth; as time increases, this growth accelerates and shortly after $t = 0.225$ (after approximately 227 time steps) the numerical scheme failed to converge. Ultimately the flow on the right side of the separation region develops such a severe variation (Ersoy & Walker 1985*b*) that the numerical mesh becomes inadequate. This behaviour is similar to that observed in two-dimensional vortex-driven flows (Walker 1978; Doligalski & Walker 1984) and is strongly suggestive that the boundary layer is evolving rapidly towards a state of interaction with the outer inviscid flow. The numerical results (Ersoy & Walker 1985*b*) suggest the development of a singular behaviour in the boundary-layer solution at finite time; a singularity is known to occur in certain two-dimensional flows (Van Dommelen 1981; Van Dommelen & Shen 1980; Elliot, Smith & Cowley 1983) as a boundary-layer flow evolves toward an interactive state. The failure of the numerical scheme is believed to occur as a consequence of the attempt to impose the tangential velocities induced by the moving vortex loop on the boundary-layer flow for an indefinite period of time. At present, numerical methods which would allow for the computation of the strong viscous–inviscid interaction that is expected to occur here are not available. However, based on the results of experimental observations (Harvey & Perry 1971; R. E. Falco 1979, private communication; Falco 1982; Falco & Wiggert 1980; Mehta & Lim 1984), it is relatively safe to say that a strong interaction is expected in this flow in the form of a boundary-layer eruption; furthermore this eruption is known to result in the ejection of a secondary three-dimensional vortex from the boundary layer.

For the second case considered, the vortex ring is initially started at an angle of attack of $\alpha = 80°$. However, until the vortex loop is relatively close to the wall, the boundary-layer development is gradual and to avoid a lengthy boundary-layer calculation, the vortex was started closer to the wall than in case 1 (see table 1). In figure 8(*a*) the instantaneous streamlines in the symmetry plane at $t = 0.1$ are depicted. Note that there are two stagnation points on the wall and these are a node of attachment S1 and a node of separation S2, which at this stage is out of the plot window (cf. figure 8*a*) to the left. The flow field at this stage is almost symmetric

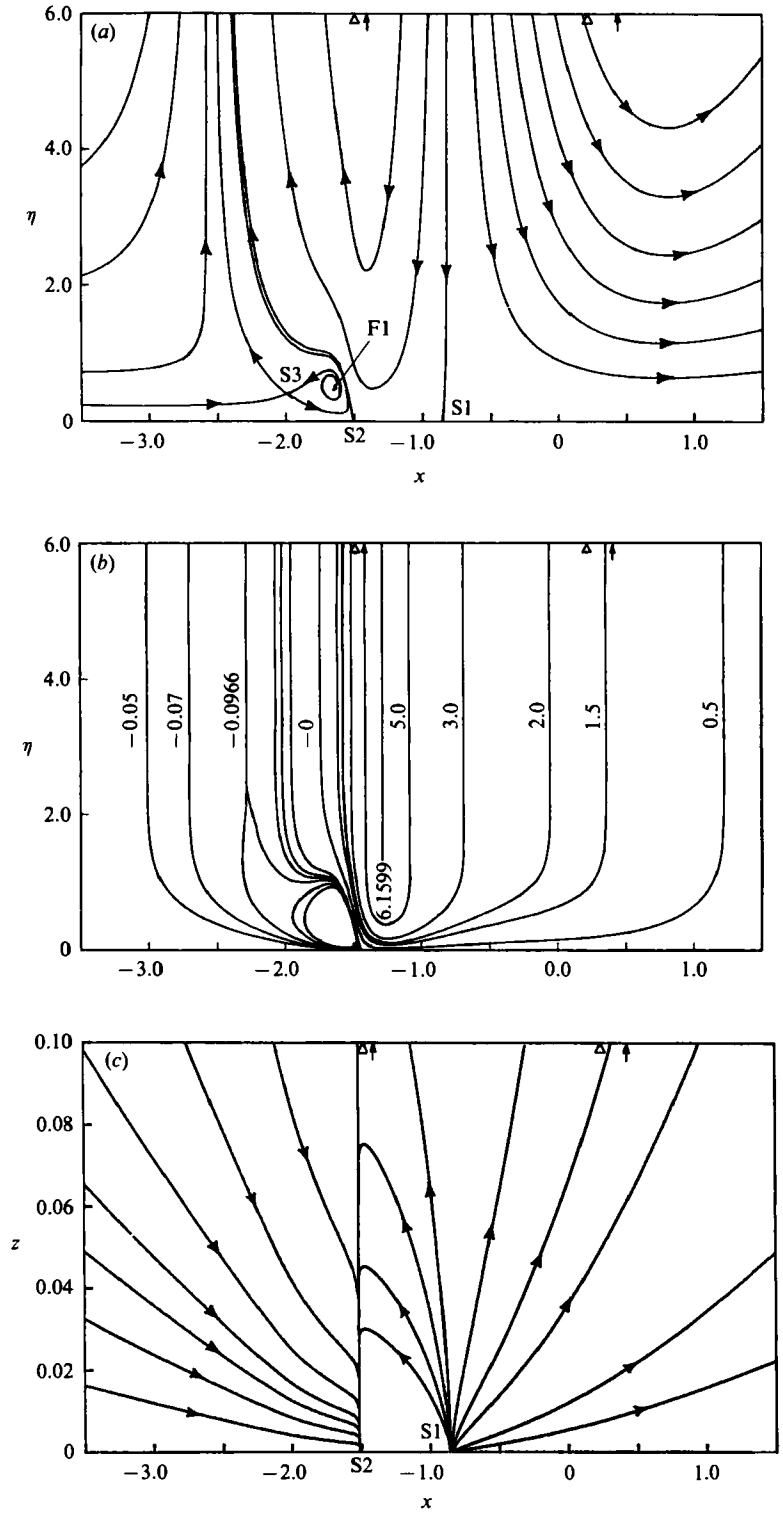

FIGURE 6. Boundary-layer development at $t = 0.175$ for case 1. (*a*) Streamlines in the symmetry plane; (*b*) constant-θ contours; (*c*) limiting surface streamlines in the (x, z)-plane.

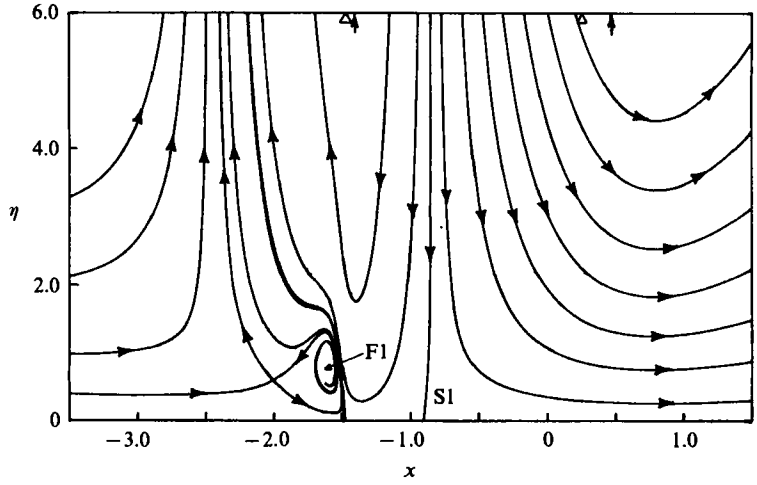

FIGURE 7. Streamlines in the symmetry plane for case 1 at $t = 0.2$.

about the limiting streamline through S1 although a slight lifting of the streamlines near $x = -1.5$ may be observed. Contours of constant θ at $t = 0.1$ are depicted in figure 8(*b*); here all values of θ are positive, indicating that for x- and y-locations within the plot window, the spanwise flow is away from the symmetry plane. It should be noted however that for larger negative values of x to the left of the plot window, there are contours of negative (but small) values of θ; in this region, there is a weak spanwise inflow towards the symmetry plane. The constant curves in figure 8(*b*) are divided into three regions by the limiting contour $\theta = 2.4964$; to the left and right of $x = 0$ there are two pockets contained by the limiting contour within which the largest values of θ are achieved. The left pocket contains the higher values of θ because the lower portion of the vortex loop is closer to the wall for $x < 0$.

The next stage of development for case 2 is shown in figure 9 at $t = 0.175$. It may be observed in figure 9(*a*) that a small region of three-dimensional separation has occurred near the wall for $x < 0$; the streamwise extent of this separation is delineated by the two stagnation points S3 and S4 in figure 9(*a*). Note that this type of separation is somewhat different than observed in case 1. The stagnation point S4 is a node of separation and the limiting streamline through S4 bends to the left and ultimately rises towards the inviscid-flow region. The stagnation point S3 is a saddle point of attachment and the limiting streamline through S3 originates at the focus F1 and spirals outward. All other streamlines near F1 spiral outward and ultimately pass between the wall and the limiting streamline through S4. The focus F1 is a point where the instantaneous flow enters the symmetry plane from outside and continuity requires that θ be negative so that there is a spanwise inflow near F1. It may be observed from figure 9(*b*) that the separation in the symmetry plane has been accompanied by the evolution of a pocket of negative θ-values near $x = -1.5$; this region of negative θ overlays and is somewhat larger than the separation region bounded by S3 and S4 in figure 9(*a*). Note that the $\theta = 0$ contour has now penetrated the plot window from the left and intersects the wall near $x = -2.1$.

The surface streamlines at $t = 0.175$ are plotted in figure 9(*c*) and show a considerable change from figure 8(*c*). The surface streamlines which emanate from the stagnation point S1 are ultimately deflected in the region to the left of S1 into a streamline which is perpendicular to the symmetry plane for small z and which

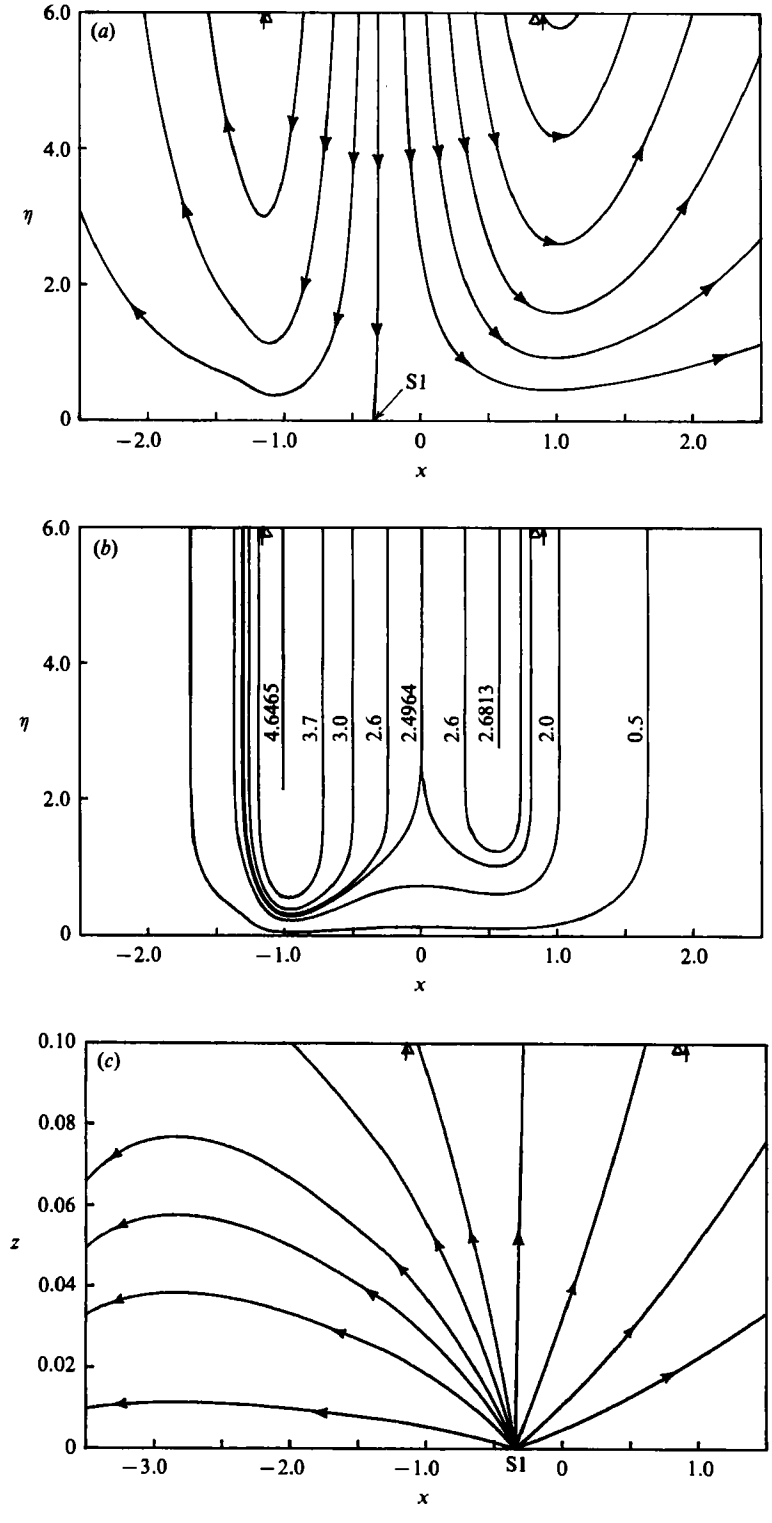

FIGURE 8. Boundary-layer development at $t = 0.1$ for case 2. (*a*) Streamlines in the symmetry plane; (*b*) constant-θ contours; (*c*) limiting surface streamlines in the (x, z)-plane.

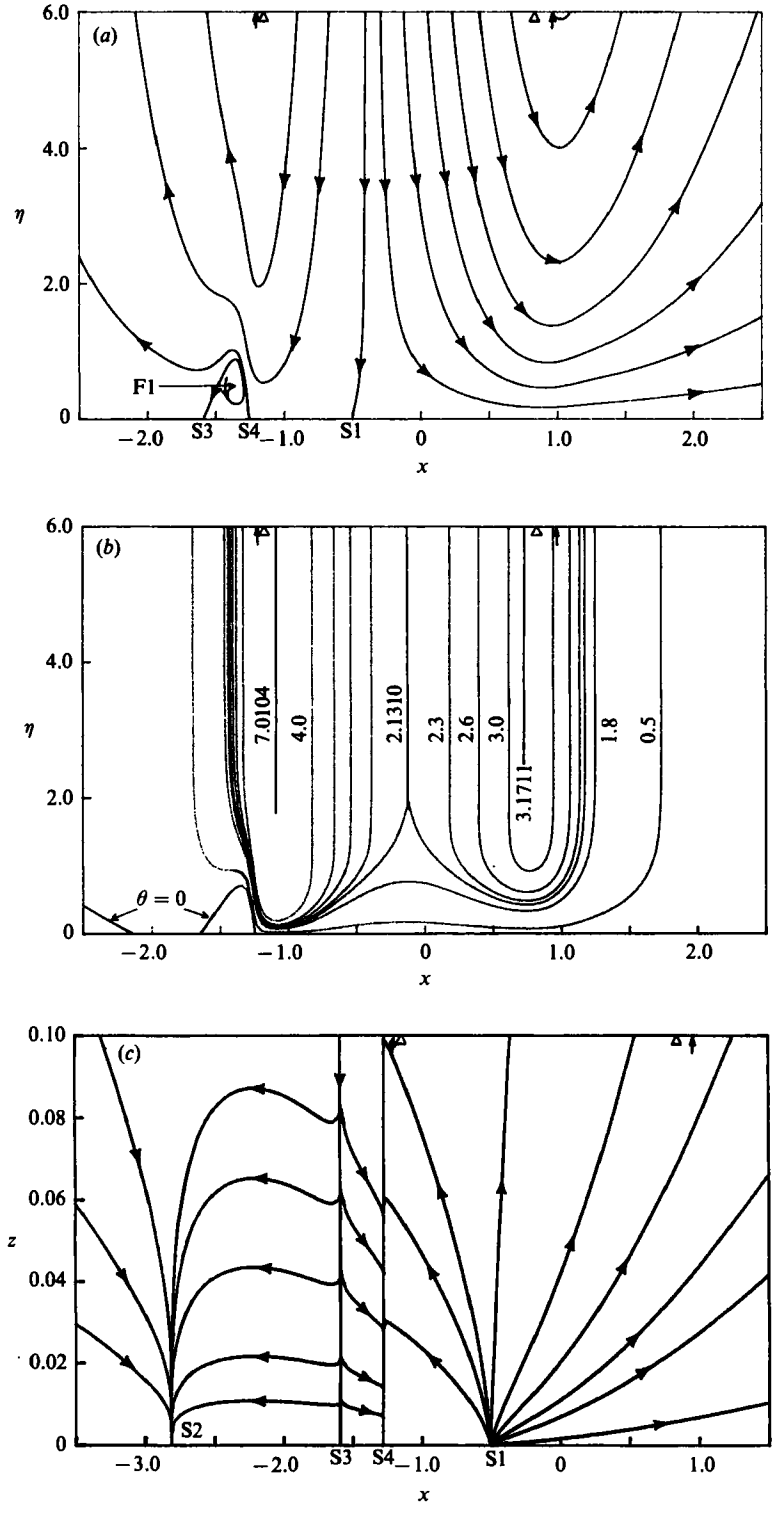

FIGURE 9. Boundary-layer development at $t = 0.175$ for case 2. (*a*) Streamlines in the symmetry plane; (*b*) constant-θ contours; (*c*) limiting surface streamlines in the (x, z)-plane.

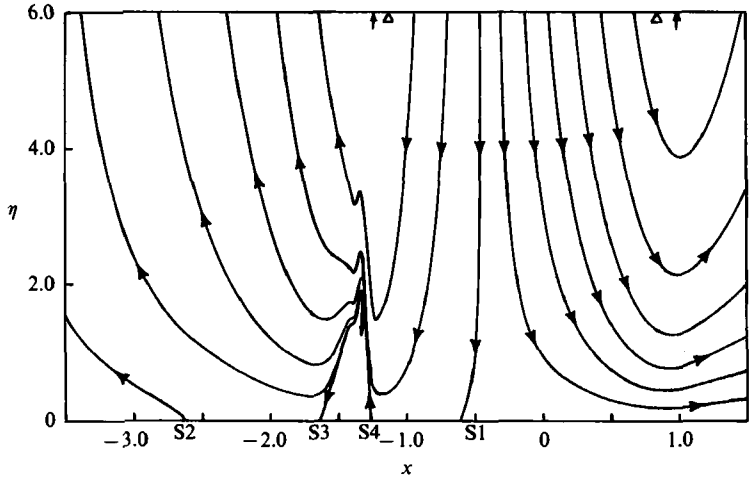

FIGURE 10. Streamlines in the symmetry plane at $t = 0.2$ for case 2.

terminates at S4; the stagnation point S4 is a node of separation and here the flow is away from the wall. Between S3 and S4, the surface streamlines move from the limiting streamline through S3 to the streamline terminating at S4. The stagnation point S3 is a saddlepoint of attachment. It may be seen that just to the left and right of S3 and S4 respectively there are small regions of inflow towards the symmetry plane; for this reason, the small zone of negative θ in figure 9(*c*) is somewhat larger in streamwise extent than the region of separation between S3 and S4 in figure 9(*a*). To the left of S3, the surface streamlines converge towards the node of separation S2 at $x = -2.8$. Note that the surface streamline patterns depicted in figure 9(*c*) apply only near the plane of symmetry since this is the only information produced in the present approach. The patterns depicted in figure 9(*c*) can only be continued to $O(1)$ distances from the symmetry plane by carrying out a full three-dimensional boundary-layer integration.

As time increases an intense variation develops on the right side of the separation in figure 9(*a*) and the $\theta = 0$ line in figure 9(*b*). By this stage, the boundary layer is in a state of rapid local growth at streamwise locations near S4 and shortly after $t = 0.2$ (after over 200 time steps) the integrations failed to converge. The streamlines in the symmetry plane at $t = 0.2$ (just before failure) are depicted in figure 10. Note that the stagnation point S2 has now moved into the plot window from the left. The kinking and severe distention of the streamlines as well as the severe boundary-layer growth near S4 are again suggestive of the early stages of the development of a singular behaviour in the boundary-layer solution. It is expected that this flow will also become interactive with the outer inviscid flow and further that the interaction will involve the ejection of some type of secondary vortex structure from the boundary-layer region.

The final case considered here corresponds to a vortex which has the opposite rotation to the vortices considered in cases 1 and 2 and which therefore recedes from the wall. The vortex ring was initially situated at a distance of $l = 1.444$ from the wall and at an angle of attack of $\alpha = 70°$. The instantaneous streamlines in the symmetry plane are plotted in figure 11(*a*) at $t = 0.2$. The stagnation point S1 is now characterized by flow away from the wall and the limiting streamline through S1 is now inclined to the left. A second stagnation point S2 is located for $x < 0$ out of the

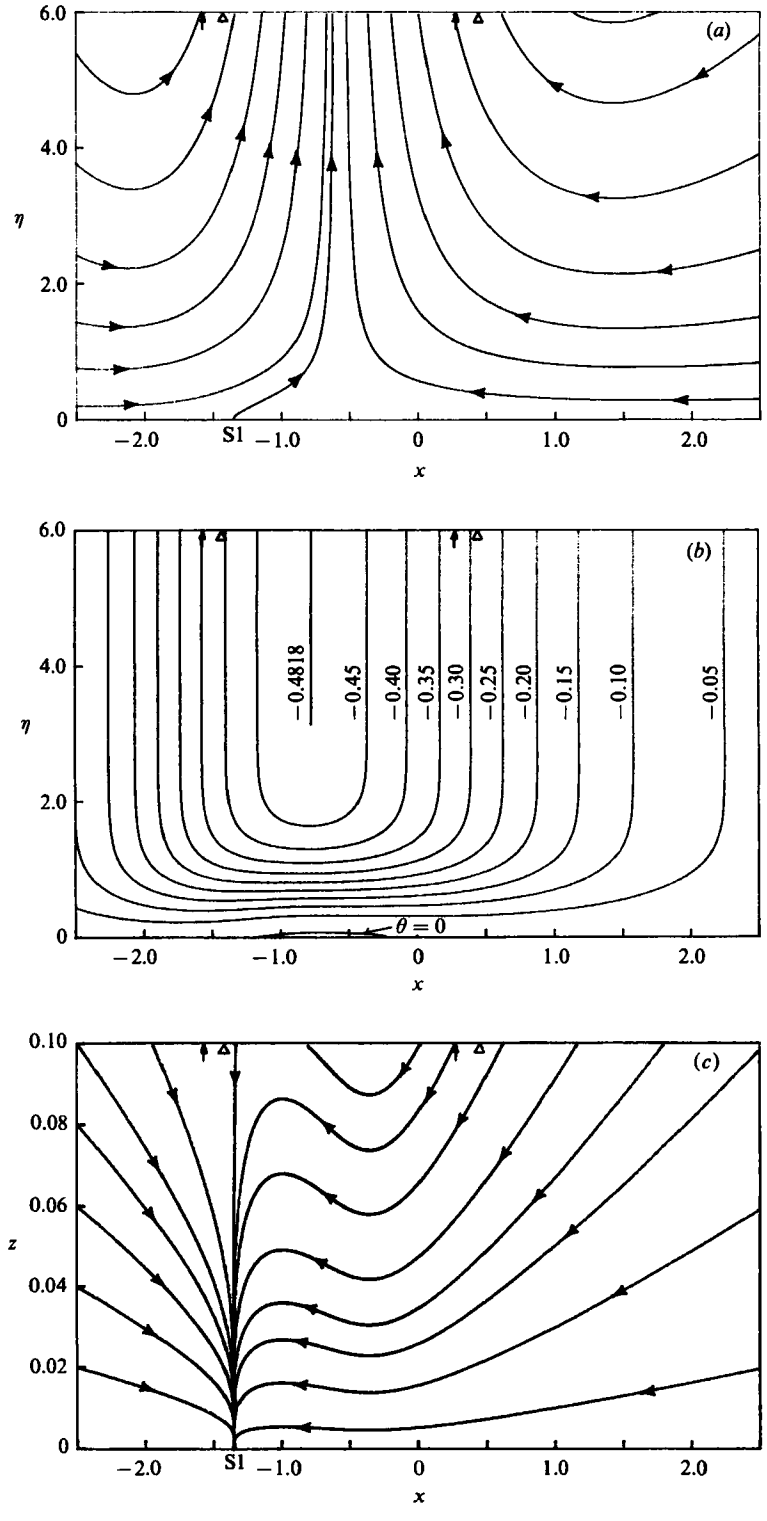

FIGURE 11. Boundary-layer development at $t = 0.2$ for case 3. (*a*) Streamlines in the symmetry plane; (*b*) constant-θ contours; (*c*) limiting surface streamlines in the (x, z)-plane.

plot window to the left and is characterized by flow toward the wall. At this stage, boundary-layer separation has not occurred even after 200 time steps; this is because the vortex was initially started relatively far from the wall and as the vortex recedes from the wall, the influence of the vortex progressively diminishes.

Contours of constant θ at $t = 0.2$ are plotted in figure 11(*b*) where it may be observed that the values of θ are predominantly negative, indicating that the spanwise flow induced by the vortex is towards the symmetry plane throughout the majority of the boundary layer. However near the wall, in the region $-1 < x < -0.3$, a region of positive θ has developed and here the direction of the spanwise flow is away from the plane of symmetry. The surface streamlines at $t = 0.2$ are shown in figure 11(*c*) where it may be seen that the streamlines are converging towards the node of separation S1. Note the bending of the surface streamlines to the right of S1 indicating regions of spanwise outflow from the symmetry plane; this behaviour is consistent with the region of positive θ depicted in figure 11(*c*).

The next stage of development for case 3 at $t = 0.3$ is shown in figure 12. The instantaneous streamlines in the symmetry plane are shown in figure 12(*a*); the stagnation point S1 has shifted further to the left and in addition to S2 (which is out of the plot window to the left) there are now two more stagnation points on the wall. The first of these, S3, is a node of attachment; the limiting streamline through S3 originates at upstream infinity. The second stagnation point, S4, is a saddlepoint of detachment and the limiting streamline through S4 originates at the wall and spirals towards a focus F1. The focus F1 is in a region of positive θ which may be verified with reference to figure 12(*b*). All streamlines between the wall and the limiting streamline through S3 ultimately spiral towards the focus at F1, where the instantaneous flow leaves the symmetry plane. This region may also be considered to be a region of three-dimensional separation. It may also be observed that the streamline above $x = -1$ is deforming into a pocket and this suggests that a new feature will ultimately appear in this region. Note also that the region of positive θ near the wall depicted in figure 12(*b*) is expanding. The surface streamlines at $t = 0.3$ are depicted in figure 12(*c*). For the node S1, the surface flow approaches the symmetry plane along a limiting streamline which is perpendicular to $z = 0$ for small z; for the saddle point S4 the surface flow moves away from $z = 0$ along a line which is perpendicular to $z = 0$. All surface streamlines from the node S3 diverge and move towards the limiting streamlines through S1 and S4.

The next stage of development for case 3 is shown in figure 13 at $t = 0.45$. It may be observed in figure 13 that the stagnation point S3 has moved further to the left while S4 has moved to the right. The region of three-dimensional separation bounded by S3 and S4 has expanded in the streamwise direction and grown in a direction normal to the wall. In addition, a second region of 'separation' has developed above $x = -1$; a new saddlepoint stagnation point S5 above the wall may be seen as well as new focus F2. It emerges (Ersoy & Walker 1985*b*) that F2 is in a region of negative θ; thus the spanwise flow is towards F2 in the symmetry plane and here fluid enters the plane instantaneously. All streamlines near F2 spiral outward and ultimately turn upward towards the inviscid flow region in a corridor bounded by the limiting streamlines through S5.

In this case, the numerical integrations can apparently be carried on for some time without evidence of eruptive boundary-layer growth; the present calculations were terminated after 450 time steps.

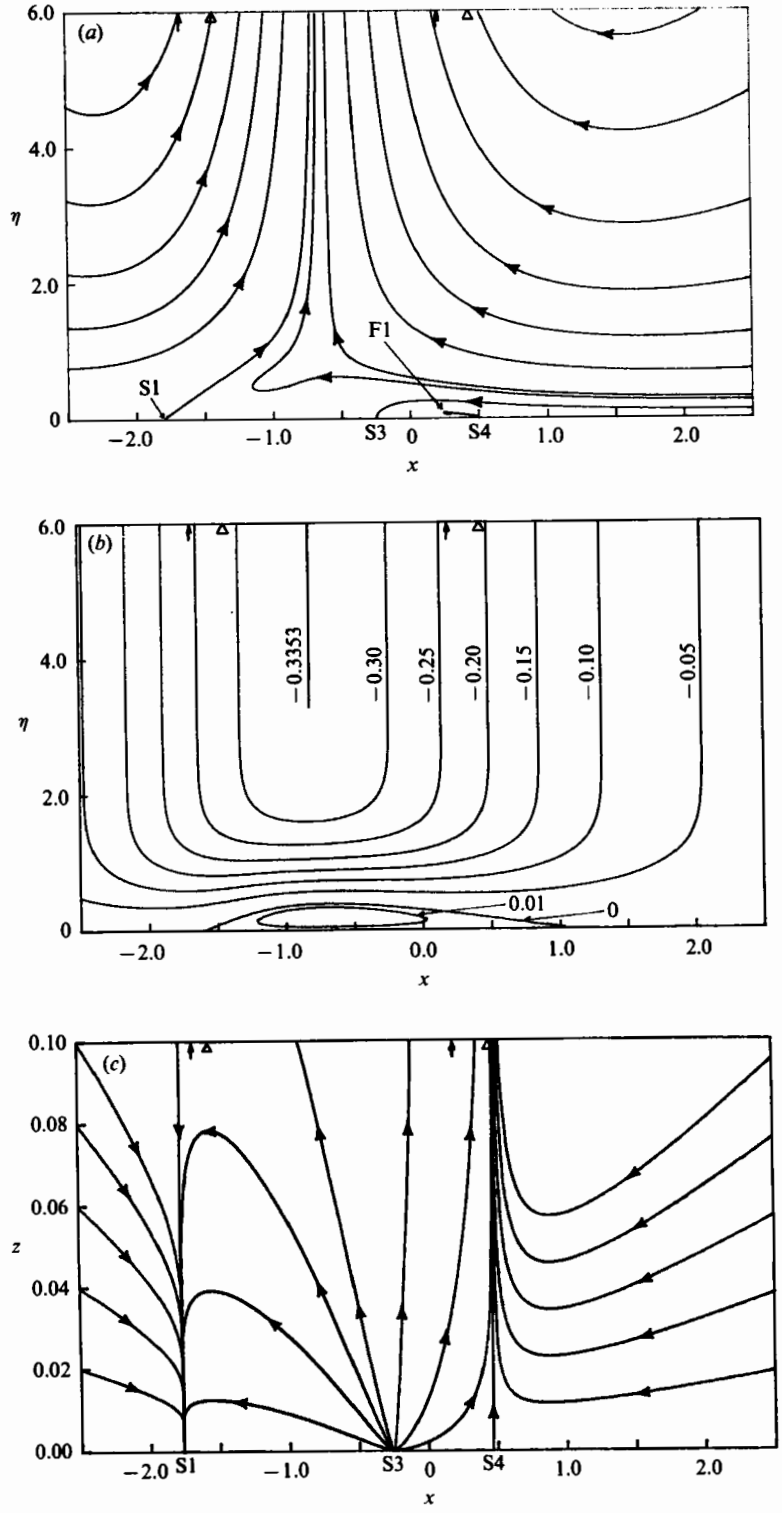

FIGURE 12. Boundary-layer development at $t = 0.3$ for case 3. (*a*) Streamlines in the symmetry plane; (*b*) constant-θ contours; (*c*) limiting surface streamlines in the (x, z)-plane.

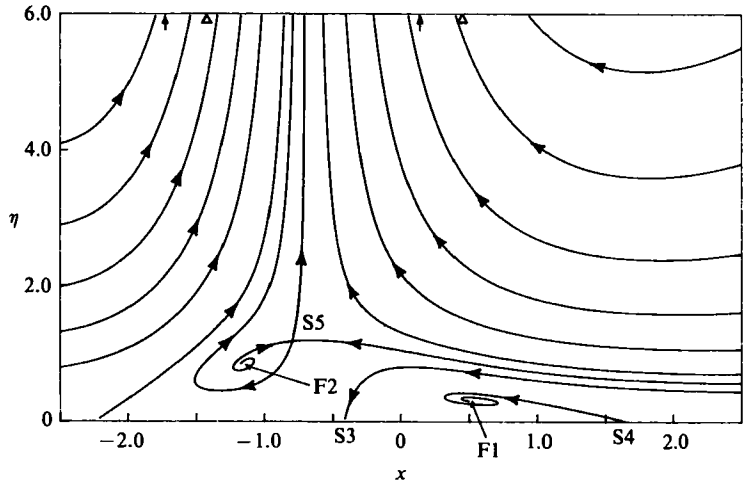

FIGURE 13. Streamlines in the symmetry plane at $t = 0.45$ for case 3.

7. Discussion

In this paper, detailed results have been presented for the boundary-layer development induced by a moving three-dimensional vortex loop above a plane wall in an otherwise stagnant fluid. The procedure outlined here allows the computation of the velocity components on and near the plane of symmetry of the vortex loop; in principle, the procedure may be extended to other unsteady three-dimensional flow situations where a plane of symmetry exists.

In the first two cases considered, the circulation of the vortex loop was selected so that the vortex moved towards the wall. The calculated results for the flow near the symmetry plane show that boundary-layer separation occurs rapidly in the region where the vortex loop is closest to the wall. This boundary-layer separation bears some similarity to the two-dimensional separations induced by a moving vortex pair (Ersoy & Walker 1986) but in general is much more complex. In particular the instantaneous streamlines in the symmetry plane do not generally form closed paths in the region of separation; in the present study, the streamlines generally consisted of a spiral motion towards a focus at which fluid was either instantaneously entering or leaving the plane of symmetry. Note that since the u- and v-velocities computed in the present study describe the flow close to the symmetry plane to within an error $O(z^2)$ and since w is known within an error $O(z^3)$, it has been possible to obtain a clear picture of the three-dimensional flow characteristics near the symmetry plane.

The numerical results for the first two cases show the development of separation phenomena in three dimensions which are rather different. However both cases ultimately show an explosive boundary-layer growth near the separation region and suggest that a boundary-layer eruption will occur for all such flows where a vortex loop with positive circulation Γ approaches a wall. It should be emphasized that the calculations reported here only describe the flow development near the symmetry plane. It is entirely possible that the onset of a boundary-layer eruption may first develop at spanwise locations away from the symmetry plane; this point can only be resolved through a calculation of the entire three-dimensional boundary-layer flow. The precise nature of the expected eruption and the subsequent strong viscous–inviscid interaction that will ensue could not be computed in this study.

However, it is anticipated that the interaction will involve the ejection of some type of secondary vortex from the boundary layer and this expectation appears to be compatible with experimental observations (R. E. Falco 1979, private communication; Falco 1982; Falco & Wiggert 1980).

For case 3, where $\Gamma < 0$ and the vortex loop recedes from the wall, boundary-layer separation also occurs. This separation also bears a resemblance to that induced by a pair of rectilinear vortices which recede from a wall (Ersoy & Walker 1986) but again the three-dimensional separation is much more complex. For case 3, the boundary-layer integrations could be carried on for a relatively long period of time without any evidence of the onset of explosive boundary-layer growth. In this situation, the vortex is initially far enough away from the wall so that it is able to 'escape' the wall region without inducing a boundary-layer eruption. There is a parallel to this behaviour in the two-dimensional flow induced by a rectilinear vortex pair which recedes from the wall (Ersoy & Walker 1985*a*). It is to be expected (on the basis of the two-dimensional results, Ersoy & Walker 1986) that if the vortex ring were started closer to the wall (with $\Gamma < 0$), explosive boundary-layer growth and a strong interaction would be induced before the vortex loop can escape the wall region.

The authors wish to express their appreciation to the Air Force of Scientific Research for supporting this study under AFOSR contract number F49620-83-K-0033.

REFERENCES

ACARLAR, M. S. & SMITH, C. R. 1984 An experimental study of hairpin vortices as a potential flow structure of turbulent boundary layers. *Rep.* FM-5. Department of Mechanical Engineering and Mechanics, Lehigh University.

ACARLAR, M. S. & SMITH, C. R. 1987*a* A study of hairpin vortices in a laminar boundary layer. Part 1. Hairpin vortices generated by a hemisphere protruberance. *J. Fluid Mech.* **175**, 1–41.

ACARLAR, M. S. & SMITH, C. R. 1987*b* A study of hairpin vortices in a laminar boundary layer. Part 2. Hairpin vortices generated by fluid injection. *J. Fluid Mech.* **175**, 43–83.

BATCHELOR, G. K. 1970 *An Introduction to Fluid Dynamics.* Cambridge University Press.

BIPPES, H. 1972 *Sitzungber. Heidel. Akad. Wiss. Math. Naturwiss.* **K1**, 103.

CALLEGARI, A. J. & TING, L. 1978 Motion of a curved vortex filament with decaying vortical core and axial velocity. *SIAM J. Appl. Maths* **35**, 148–174.

CERRA, A. W. & SMITH, C. R. 1983 Experimental observation of vortex ring interaction with fluid adjacent to a surface. *Rep.* FM-4. Department of Mechanical Engineering and Mechanics, Lehigh University.

DHANAK, M. R. 1981 Interaction between a vortex filament and an approaching rigid sphere. *J. Fluid Mech.* **109**, 129–147.

DHANAK, M. R. & DE BERNARDINIS, B. 1981 The evolution of an elliptic vortex ring. *J. Fluid Mech.* **109**, 189–216.

DIDDEN, N. & HO, C.-M. 1985 Unsteady separation in a boundary layer produced by an impinging jet. *J. Fluid Mech.* **160**, 235–256.

DOLIGALSKI, T. L. & WALKER, J. D. A. 1978 Shear layer breakdown due to vortex motion. In *Proc. Workshop on Coherent Structure of Turbulent Boundary Layers* (ed. C. R. Smith & D. E. Abbott), pp. 288–339. Lehigh University.

DOLIGALSKI, T. L. & WALKER, J. D. A. 1984 The boundary layer due to a convected two-dimensional vortex. *J. Fluid Mech.* **139**, 1–28.

ELLIOT, J. W., SMITH, F. T. & COWLEY, S. J. 1983 Breakdown of boundary layers: (i) on moving surfaces; (ii) in semi-similar unsteady flow; (iii) in fully unsteady flow. *Geophys. Astrophys. Fluid Dyn.* **25**, 77–138.

ERSOY, S. & WALKER, J. D. A. 1985*a* Viscous flow induced by counter-rotating vortices. *Phys. Fluids* **28**, 2687–2698.

ERSOY, S. & WALKER, J. D. A. 1985*b* The viscous flow induced near a wall by counter-rotating vortex pairs and vortex loops. *Rep.* FM-8. Department of Mechanical Engineering and Mechanics, Lehigh University.

ERSOY, S. & WALKER, J. D. A. 1986 The flow induced at a wall by a vortex pair. *AIAA J.* **24**, 1597–1605.

FALCO, R. E. 1977 Coherent motions in the outer region of a turbulent boundary layer. *Phys. Fluids* **20**, S124–S132.

FALCO, R. E. 1982 A synthesis and model of turbulence structure in the wall region. In *Structure of Turbulence in Heat and Mass Transfer* (ed. Z. P. Zaric), Hemisphere.

FALCO, R. E. 1983 New results, a review and synthesis of the mechanism of turbulence production in boundary layers and its modification. *AIAA Paper* 83-0377.

FALCO, R. E. & WIGGERT, D. C. 1980 The effects of dilute polymer additives on vortex ring/wall interactions – a mechanism for drag reduction. In *Viscous Flow Drag Reduction* (ed. G. Hough), *Prog. Astronaut. Aeronaut.* **72**, 275–289.

HARVEY, J. K. & PERRY, F. J. 1971 Flowfield produced by trailing vortices in the vicinity of the ground. *AIAA J.* **9**, 1659–1660.

HEAD, M. R. & BANDYOPHADYAY, P. 1981 New aspects of turbulent boundary-layer structure. *J. Fluid Mech.* **107**, 297–337.

HON. L.-T. & WALKER, J. D. A. 1987 An analysis of motion and effects of hairpin vortices. *Rep.* FM-11. Department of Mechanical Engineering and Mechanics, Lehigh University.

LAMB, H. 1932 *Hydrodynamics.* Cambridge University Press.

LEONARD, A. 1980 Vortex methods for flow simulation. *J. Comp. Phys.* **37**, 289–335.

LEONARD, A. 1985 Computing three-dimensional incompressible flows with vortex filaments. *Ann. Rev. Fluid Mech.* **17**, 523–559.

LIGHTHILL, M. J. 1963 Boundary layer theory. In *Laminar Boundary Layers* (ed. L. Rosenhead), pp. 46–109. Oxford University Press.

MEHTA, R. D. & LIM, T. T. 1984 Flow visualization study of a vortex/wing interaction. *NASA Tech. Memo.* 86656.

MOORE, D. W. 1972 Finite amplitude waves on aircraft trailing vortices. *Aero. Q.* **23**, 307–314.

MOORE, D. W. & SAFFMAN, P. G. 1972 The motion of a vortex with axial flow. *Phil. Trans. R. Soc. Lond.* A**272**, 403–429.

SMITH, C. R. 1984 A synthesized model of the near-wall behavior in turbulent boundary layers. In *Proc. Eighth Bienniel Symp. on Turbulence* (ed. G. K. Patterson & J. L. Zakin), pp. 299–325. University of Missouri-Rolla, Missouri.

VAN DOMMELEN, L. L. 1981 Unsteady boundary layer separation. Ph.D. dissertation, Cornell University.

VAN DOMMELEN, L. L. & SHEN, S. F. 1980 The spontaneous generation of a singularity in a separating laminar boundary layer. *J. Comp. Phys.* **38**, 125–140.

WALKER, J. D. A. 1978 The boundary layer due to a rectilinear vortex. *Proc. R. Soc. Lond.* A**359**, 167–188.

WALKER, J. D. A., SCHARNHORST, R. K. & WEIGAND, G. G. 1986 Wall layer models for the calculation of velocity and heat transfer in turbulent boundary layers. *AIAA Paper* 86-0213, Reno, Nevada; to appear in *AIAA J.*

WALKER, J. D. A., SMITH, C. R., CERRA, T. & DOLIGALSKI, T. L. 1987 The impact of a vortex ring on a wall. *J. Fluid Mech.* **181**, 99–140.